Laser melting modes in metal powder bed fusion additive manufacturing

Cang Zhao,* Bo Shi, Shuailei Chen, and Dong Du

Department of Mechanical Engineering, Tsinghua University, Beijing 100084, China,
Key Laboratory for Advanced Materials Processing Technology, Ministry of Education, Beijing 100084, China,
and Beijing Key Lab of Precision/Ultra-precision Manufacturing Equipments and Control, Tsinghua University, Beijing 100084, China

Tao Sun

Department of Materials Science and Engineering, University of Virginia, Charlottesville, Virginia 22904, USA

Brian J. Simonds

Applied Physics Division, Physical Measurements Laboratory, National Institute of Standards and Technology, Boulder, Colorado 80305, USA

Kamel Fezzaa

X-ray Science Division, Argonne National Laboratory, Lemont, Illinois 60439, USA

Anthony D. Rollett

Department of Materials Science and Engineering, Carnegie Mellon University, Pittsburgh, Pennsylvania 15213, USA
and Next Manufacturing Center, Carnegie Mellon University, Pittsburgh, Pennsylvania 15213, USA

(published 20 October 2022)

In the laser powder bed fusion additive manufacturing of metals, extreme thermal conditions create many highly dynamic physical phenomena, such as vaporization and recoil, Marangoni convection, and protrusion and keyhole instability. Collectively, however, the full set of phenomena is too complicated for practical applications and, in reality, the melting modes are used as a guideline for printing. With an increasing local material temperature beyond the boiling point, the mode can change from conduction to keyhole. These mode designations ignore laser-matter interaction details but in many cases are adequate to determine the approximate microstructures, and hence the properties of the build. To date no consistent, common, and coherent definitions have been agreed upon because of historic limitations in melt pool and vapor depression morphology measurements. In this review, process-based definitions of different melting modes are distinguished from those based on postmortem evidence. The latter are derived mainly from the transverse cross sections of the fusion zone, whereas the former come directly from time-resolved x-ray imaging of melt pool and vapor depression morphologies. These process-based definitions are more strict and physically sound, and they offer new guidelines for laser additive manufacturing practices and create new research directions. The significance of the keyhole, which substantially enhances the laser energy absorption by the melt pool, is highlighted. Recent studies strongly suggest that stable-keyhole laser melting enables efficient, sustainable, and robust additive manufacturing. The realization of this scenario demands the development of multiphysics models, signal translations from morphology to other feasible signals, and in-process metrology across platforms and scales.

DOI: 10.1103/RevModPhys.94.045002

CONTENTS

*cangzhao@tsinghua.edu.cn

I. INTRODUCTION

Metal additive manufacturing (AM), commonly referred to as 3D printing, is an industrial application of rapid prototyping of metal parts (Kruth, Leu, and Nakagawa, 1998; Campbell, Bourell, and Gibson, 2012). It was originally derived from the alliance of welding methods and powder-based technologies. The direct powder deposition into a laser melted pool gave rise to direct laser fabrication and laser engineered net shaping technologies (Lewis *et al.*, 1994; Griffith *et al.*, 1996; Atwood *et al.*, 1998; Lewis and Schlienger, 2000) that, while effective, lacked the resolution to be generally useful without post machining and were not helped by a low deposition rate. Once the original patents had expired, however, the development of powder bed systems quickly revealed that good resolutions and reasonable build rates enabled the direct manufacturing of complex geometries and almost fully dense parts. It was this development that took 3D printing from the status of rapid prototyping to actual additive manufacturing of end-use products.

Metal AM, by definition, is a collection of disruptive technologies that fabricate metal parts directly from digital computer-aided design and drafting models, usually layer upon layer (ASTM International, 2021). In comparison to conventional subtractive or formative manufacturing, this emerging cluster offers unprecedented design freedom and manufacturing capabilities for multiscale, multimaterial, and multifunctional optimization and integration (Frazier, 2014; Herzog *et al.*, 2016; MacDonald and Wicker, 2016; Onuike, Heer, and Bandyopadhyay, 2018; Leach *et al.*, 2019; Gu *et al.*, 2021; Sing *et al.*, 2021). In addition, metal AM requires a short supply chain, which becomes increasingly critical when one considers global supply chain disruption risks (Thomas, 2016; Kurpjuweit *et al.*, 2021). The on-site and on-demand manufacturing capability can largely reinforce economic and societal resilience and sustainability. As a result, metal AM has been evolving rapidly during the past decade and is transforming the aeronautic, aerospace, automotive, defense, chemical, medical, and energy industries (Martin *et al.*, 2017; Gisario *et al.*, 2019; Joint Defense Manufacturing Council, 2021). Here are a few examples. Topologically optimized components such as graded lattice structures can be built via metal AM to largely reduce the buy-to-fly ratio (weight ratio of raw material and final part) of an aircraft (Gaynor and Guest, 2016; Maconachie *et al.*, 2019). Sensors and actuators can be seamlessly embedded in a component for structural health monitoring and assessment (Hossain *et al.*, 2016; Juhasz *et al.*, 2020). Metal implants customized to individual patients can be quickly built using AM, and it is now possible to tailor the elastic modulus and stiffness to mimic human bone (Sing *et al.*, 2016; Wang *et al.*, 2016).

Of all the competing metal AM technologies, laser powder bed fusion (LPBF), also known as selective laser melting, is currently the most commonly used (Thijs *et al.*, 2010; Frazier, 2014; Khairallah *et al.*, 2016; Zhao *et al.*, 2020). In a LPBF process, a laser beam of high power density is scanned across a thin layer of metal powder (less than 100 μm thickness) to locally and selectively melt the powder and fuse it to a previous layer. Typically, spherical powder particles are favored because of their high flowability, which improves powder bed uniformity and part quality (Heiden *et al.*, 2019; Brika *et al.*, 2020). Benefiting from the small sizes of the laser beam ($\sim$100 μm) and the powder particles (typically $10-60$ μm) and a correspondingly small melt pool width ($\sim$200 μm in the transverse direction), LPBF enables high dimensional accuracy and extreme flexibility in fabricating complex features and structures (Wu, Narra, and Rollett, 2020; Seltzman and Wukitch, 2021). The high cooling rates (10^6 K/s) associated with the small melt pool and fast laser scanning promote high solidification rates, which refines the grains and opens up new avenues and opportunities for developing innovative materials with far-from-equilibrium phases and improved properties, for example, new alloys that work under extremely harsh environments (such as space, deep oceans, and nuclear plants) where extreme temperatures, pressures, shocks, radiation, or corrosion exists (Kyo *et al.*, 1995; Hou *et al.*, 2020; Mohr *et al.*, 2020; McEnerney *et al.*, 2021). Furthermore, the digital nature of LPBF allows flexible control of processing conditions during the build of a single part. When using the same laser parameters, the uniform processing condition throughout the part eliminates much of the variability with casting, such as macrosegregation (Wang *et al.*, 2017; Agrawal *et al.*, 2020). When one implements various parameters, the material microstructures can be adjusted at various locations of the part, offering enhanced performance induced by the heterogeneity (Sun *et al.*, 2019; Sofinowski *et al.*, 2021).

LPBF is effectively an extension of laser welding on a small scale, which means, however, that it is subject to many of the same limitations. For example, LPBF parts are vulnerable to hot cracking due to dendritic growth during solidification and substantial residual stress (Martin *et al.*, 2017; Zhang *et al.*, 2017). This has largely limited the range of compositions to which LPBF can be applied, i.e., predominantly only to weldable alloys. Meanwhile, many aspects of the LPBF-produced microstructures differ strongly from those conventionally produced, with features such as cellular structures, high dislocation content, supersaturation, nanoprecipitation, nonequilibrium phases, inclusions, and irregular grain structures (Herzog *et al.*, 2016; Martin *et al.*, 2017; Wang *et al.*, 2018; Voisin *et al.*, 2021). Some of these unique structures are

beneficial, while others can deteriorate performance. For some alloys, the overall densities of LPBF parts are generally excellent (99.5% of the theoretical density), but the complex laser and powder conditions can generate anomalies and occasionally structural defects, such as variable melt pools, porosity, and cracks (Wu *et al.*, 2014; Chiang *et al.*, 2019; Scime and Beuth, 2019a; Dowling *et al.*, 2020; Zhao *et al.*, 2020,2022; Mostafaei *et al.*, 2022). This is one of the main factors currently hindering a wider application of LPBF in some industries. To manufacture defect-free and microstructure-controllable parts, we need a more comprehensive understanding of the interaction between laser and matter and the mode of laser melting.

In LPBF of metals, the mode of melting is one of the most fundamental concepts (Paul and Debroy, 1988; Fabbro and Chouf, 2000; King *et al.*, 2015; Cunningham *et al.*, 2019; Chen *et al.*, 2020; Zhao *et al.*, 2020). Generally, it consists of conduction and keyhole modes (Semak and Matsunawa, 1997; Rai *et al.*, 2007; King *et al.*, 2014; Aboulkhair *et al.*, 2016; Scipioni Bertoli, Wolfer *et al.*, 2017; Forien *et al.*, 2020; Jadhav *et al.*, 2021). Between these two modes, it is also often believed that there is a transition mode (Lee *et al.*, 2002; Verhaeghe *et al.*, 2009; Qi *et al.*, 2017; Simonds *et al.*, 2018; Ye *et al.*, 2019; Liu, Wang, and Yan, 2020; Tenbrock *et al.*, 2020). These modes, regardless of the absence of detailed and complicated laser-matter interactions, largely determine the microstructures and defects as well as the performances of the product (Sames *et al.*, 2016; Cunningham, Narra *et al.*, 2017; Wei, Elmer, and DebRoy, 2017; Zhao *et al.*, 2017; Liu and Shin, 2019; Sun *et al.*, 2019; Hu *et al.*, 2020; Polonsky *et al.*, 2020; Roehling *et al.*, 2020; Martin *et al.*, 2021). For example, melting in keyhole mode can potentially refine grain structure, improve material strength, and mitigate cracking; when unstable, however, it can lead to keyhole porosity and degrade corrosion resistance and fatigue life (Aboulkhair *et al.*, 2014; Cunningham, Narra *et al.*, 2017; Roehling *et al.*, 2020; Huang *et al.*, 2022).

Despite their crucial role in the previously mentioned research and development, these melting modes have not yet achieved consistent, common, and coherent definitions. This shapes the motivation for this review. Traditionally and experimentally, the postmortem transverse cross section (perpendicular to the laser path) of a fused melt pool is used to distinguish the modes (Paul and Debroy, 1988; Assuncao, Williams, and Yapp, 2012; King *et al.*, 2014; Qi *et al.*, 2017; Scipioni Bertoli, Wolfer *et al.*, 2017; Simonds *et al.*, 2018; Ye *et al.*, 2019). Such a postmortem-based approach is simple and common in the community. However, the information of the vapor depression is missing and the boundaries of the modes are subjective and confusing (King *et al.*, 2014; Simonds *et al.*, 2018). Recently the *operando* high-speed synchrotron x-ray imaging technique has enabled the community to refine and revise those long-standing definitions because of its micrometer spatial resolution, subnanosecond temporal resolution, megahertz frame rate, and millimeter penetration capacity (Zhao *et al.*, 2017; Calta *et al.*, 2018; Leung *et al.*, 2018; Miyagi *et al.*, 2018; Parab *et al.*, 2018; Martin *et al.*, 2019a; Zhao *et al.*, 2019; Hocine *et al.*, 2020). The revised definitions come directly from the time-resolved measurements of the melt pool and vapor depression morphology evolutions (Cunningham *et al.*, 2019; Chen *et al.*, 2020; Zhao *et al.*, 2020). Compared to the postmortem-based version, these process-based definitions are clearer and more strict in physics. But so far they have not attracted sufficient attention.

In this review, we employ the following terminologies when referring to the vapor-dominated cavity inside the melt pool. In general, the term "vapor depression" applies to any shape of cavity caused by the recoil momentum from vaporization of the liquid surface. It is more general and inclusive. The term "keyhole" is a subtype of the vapor depression. It comes from the welding community in the early days of deep penetration technologies (electron beam and laser beam) (Miller and Takenaka, 1964; Elmer *et al.*, 2011) but has evolved into a broader concept (Cunningham *et al.*, 2019). Traditionally, the keyhole refers to a deep and narrow vapor cavity that is derived mainly from the postmortem transverse cross section of a deep and narrow fused melt pool (Kaplan, 1994; Fabbro and Chouf, 2000; Cho and Na, 2006; Tan, Bailey, and Shin, 2013; King *et al.*, 2014; Ye *et al.*, 2019). It is somewhat of an approximation that is confined to the keyhole melting mode. Here the term keyhole is reserved for those depressions that are prone to multiple reflection, and thus increased absorption. It can be, but is not limited to, a deep and narrow morphology.

This review is presented as follows. We first describe the general physical process of laser heating. After summarizing the complexity, we review two key coupled phenomena: (1) melting and evaporation and (2) protrusion and keyhole instability. These physical phenomena drive the morphological evolution of the melt pool (with or without a vapor cavity) and are the foundation of melting mode definitions. We then assign the definitions to two categories on the basis of the morphology measurement approach. One category is based on postmortem examination and the other on *in situ* visualizations. We emphasize and encourage the latter and discuss it, in order, as *conceptual definitions*, *strict definitions*, and *from stationary to scanning*. In Sec. IV we discuss the perspectives for practical implementations of the definitions, and in Sec. V we conclude the review.

II. GENERAL PHYSICAL PROCESS OF LASER MELTING

A. Complexity

The laser melting of a metal is a highly dynamic and complicated physical process (Markl and Körner, 2016; Guo *et al.*, 2018; Kouraytem *et al.*, 2019; Zhao *et al.*, 2019; Panwisawas, Tang, and Reed, 2020; Wang, Zhang, and Yan, 2020; Zhao *et al.*, 2020). As illustrated in Fig. 1, this potentially involves all four fundamental states of matter: solid, liquid, vapor, and plasma. It also includes not only melting but also vaporization and recoil, Marangoni convection, vapor impact, multiple reflection and absorption, melt pool oscillations, protrusion and keyhole instability, etc.

It is the extreme thermal conditions caused by rapid heating that create these highly dynamic physical phenomena. Usually the heating and cooling rates are of the order of $10^3 - 10^8$ K/s (Farshidianfar, Khajepour, and Gerlich, 2016; Yang *et al.*, 2016; Scipioni Bertoli, Guss *et al.*, 2017; Zhao *et al.*, 2017; Hooper, 2018; Heigel, Lane, and Levine, 2020; Thampy *et al.*,

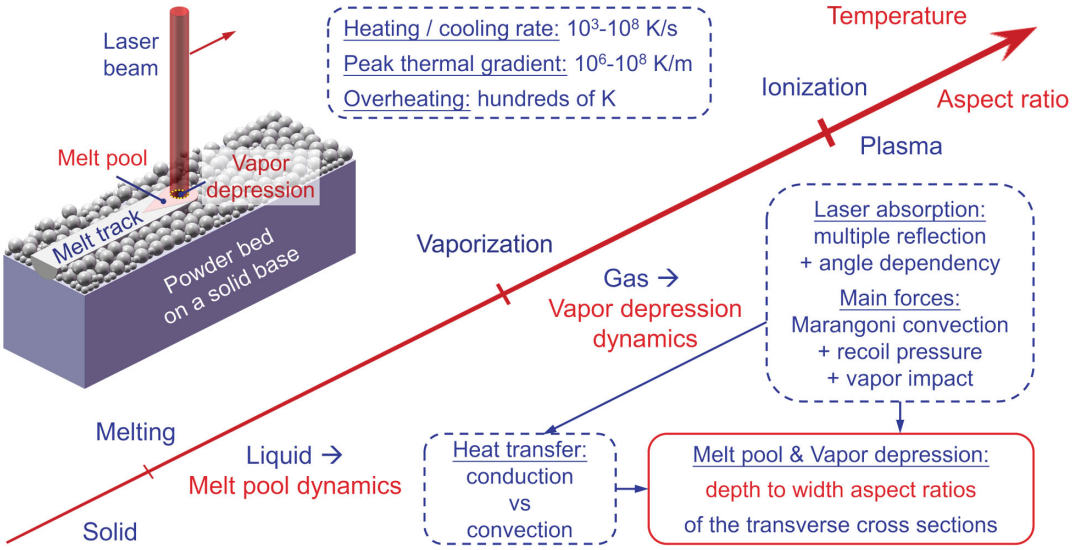

FIG. 1. The general physical process of laser melting. With the rapid increase in temperature, the solid (a powder bed sample here) transforms into liquid, gas, and plasma through the transitions of melting, vaporization, and ionization. During this process, melt pool and vapor depression form and evolve, and their depth-to-width aspect ratios of the transverse cross sections continue to rise because of enhanced laser absorption and limited heat transfer. In the schematic in the top left corner, the approximate location of the vapor depression inside the melt pool is outlined with a yellow dashed circle, while the red arrow indicates the laser scan direction.

2020), the peak thermal gradient inside the melt pool is of the order of $10^6 - 10^8$ K/m (Gäumann *et al.*, 1999; Griffith *et al.*, 1999; Bontha *et al.*, 2006; Thijs *et al.*, 2013; Hooper, 2018; Roehling *et al.*, 2020; Zhao *et al.*, 2020), and the average temperature on the vapor depression walls can be hundreds of kelvins above the boiling point of the metal (Zhao *et al.*, 2019, 2020; Pordzik and Woizeschke, 2020).

B. Melting and vaporization

1. At the atomic scale

The interaction between a high-power continuous-wave or short-duration (longer than a nanosecond) pulsed laser and a metal can be considered in terms of a balance between photon absorption and phonon emission. This process is referred to as photothermal because the absorbed energy is directly transferred into heat on that timescale (i.e., dwell time or pulse width is longer than electron-phonon or even phonon-phonon relaxation time) (Link *et al.*, 1999; El-Sayed, 2001; Brown and Arnold, 2010; Dowden, 2017). For metals, it is often the metallic bonds that join atoms through the electrostatic attraction between valence electrons and ionized cores. During the laser AM process, the rapid local heating by the high-power laser excites atomic vibrations and deforms and breaks the bonds to melt and vaporize the metal. Unlike the slow and uniform heating that occurs in an oven, metallic bond deformation and breaking under high-power laser illumination initially occurs only within a thin surface layer because of limited optical absorption depth (~10 nm) and thermal diffusion length (a few micrometers in 1 μs) (Wellershoff *et al.*, 1999; Lide, 2004; Foroozmehr *et al.*, 2016; Zhao *et al.*, 2019). The required thermal energy depends mainly on the number and strength of the bonds because of their generally isotropic nature (Campbell, 2008; Daeneke *et al.*, 2018). The bond number is associated with the material mass of the surface layer and the atomic configuration like the crystal structure of a solid phase. The bond strength is generally related to the delocalization degree of the valence electrons.

As the energy absorption increases, mostly due to single-photon interactions (Brown and Arnold, 2010), the intense collisions by free electrons enable some ionized cores to permanently move away from their equilibrium positions. The atomic motion becomes chaotic and the nonlinear multi-phonon interactions trigger phase transformations (i.e., melting or a change of crystalline phase). For example, in a pure solid metal with a coordination number of 10 (averaged over fcc and bcc crystals), melting starts when about 10% of the total metallic bonds inside the confined regime are loosened (but not yet broken). When the melting is complete, the crystal structure is completely lost and the shear modulus becomes zero, although short-range order may be preserved (Gür and Pan, 2008; Kenel *et al.*, 2017; Zhao *et al.*, 2017). In contrast, vaporization takes place only when a surface bond is broken (i.e., the kinetic energy obtained by an atom is in excess of the bond energy, on the order of a few eV), and the atoms in the vapor phase then move independently.

Under equilibrium conditions, the enthalpies required to change the phases from solid to liquid and from liquid to vapor are the latent heats of fusion and vaporization, respectively. The corresponding melting and boiling temperatures or the entropies of fusion and vaporization at a given pressure are constant. However, because of the rapid heating by the high-power laser, the actual phase transition temperatures or entropy values deviate from those characteristic points or equilibrium limits (Miotello and Kelly, 1999; Lorazo, Lewis, and Meunier, 2003; Kruth *et al.*, 2004; Ramirez-San-Juan *et al.*, 2010; Zhao *et al.*, 2019). For example, the liquid metal directly beneath the laser beam is often in a superheated state, and additional energy is required to break the bonds and

release the atoms. This situation is further complicated for multiphase alloys, in which the melting and vaporization could be highly heterogeneous as a result of the distinct strengths of the bonds between various alloy elements.

2. At the microscale

Under stationary laser-beam illumination, the metal, either plate or powder bed, is locally heated. When the temperature reaches the melting point, the metal forms a melt pool. The melt pool is initially small and shallow [Fig. 5(a)], and the heat is transported to the surrounding metal through thermal conduction (Eagar and Tsai, 1983; Assuncao, Williams, and Yapp, 2012; Panwisawas *et al.*, 2017; Zhao *et al.*, 2017). Over time, the volume of the pool increases, as does the surface temperature, because laser heating at this stage outpaces thermal diffusion (Lee *et al.*, 2002; Rai *et al.*, 2007; Gusarov and Smurov, 2010). When the temperature is above the boiling point, local boiling occurs. On the free side of the surface layer, the metal vapor is ejected mainly along the local normal direction and toward the free space. On the other side, a recoil momentum pushes the liquid below the sample surface, in the opposite direction of the vapor ejection (Semak and Matsunawa, 1997; Fabbro *et al.*, 2006; Verhaeghe *et al.*, 2009; Ly *et al.*, 2017; Bidare *et al.*, 2018; Zhao *et al.*, 2019). The flux of the vapor and the pressure of the recoil depend on the local overheating relative to the boiling point (Anisimov and Khokhlov, 1995; Semak and Matsunawa, 1997; Zhao *et al.*, 2019). Typically, for a stationary laser beam with a Gaussian profile, the surface region directly beneath the beam center achieves the highest temperature and overheating (Doubenskaia *et al.*, 2013; Yadroitsev, Krakhmalev, and Yadroitsava, 2014). As a result, the vapor is largely ejected upward and the liquid is pushed downward, creating a cavity called a vapor depression (Zhao *et al.*, 2017; Cunningham *et al.*, 2019). Generally, the melt pool and the vapor depression are nearly semicircular and symmetric. The entrance of powder particles into the laser beam or directly into the melt pool, however, could momentarily break the symmetry and create complex three-dimensional topologies (Zhao *et al.*, 2017; Wolff *et al.*, 2019; Li *et al.*, 2020; Lin *et al.*, 2020). At high power, as laser heating continues, the cavity may become deep enough that the reflected light encounters another region of the cavity interior before eventually escaping, which is colloquially referred to as multiple reflection (Kaplan, 1994; Cho and Na, 2006; Tan, Bailey, and Shin, 2013). Every time the light irradiates a melt surface, additional energy is absorbed, a fraction of which, for a given material, depends on its local angle of incidence. In the field of laser fusion AM, this phenomenon is often referred to as "Fresnel absorption." Since this term implies assumptions of how the absorption is quantified (mathematically by Fresnel equations), we prefer just "absorption" or "angle-dependent absorption" when one is referring to the phenomenon in general. Because of the positive feedback between cavity depth and laser absorption, the cavity may eventually become a deep and narrow shape (Matsunawa *et al.*, 1998; Lee *et al.*, 2002; Panwisawas *et al.*, 2017; Zhao *et al.*, 2017; Cunningham *et al.*, 2019). This was recently confirmed through real-time and simultaneous laser absorption and cavity depth measurements (Allen *et al.*, 2020). As the cavity grows, the melt pool deviates from its initially semicircular morphology in general and may show either a deep and conical shape [Fig. 5(c)] or a bimodal shape with a bowl on the top and a spike at the bottom [Fig. 4(a2)] (King *et al.*, 2014; Zhao *et al.*, 2017; Simonds *et al.*, 2018; Cunningham *et al.*, 2019). Inside the melt pool, the large thermal gradients, mostly around the vapor depression walls, promote convective mass and heat transfer. The heat transfer, though limited, confines the growth of the melt pool (Lee *et al.*, 2002; Rai *et al.*, 2007; Gusarov and Smurov, 2010).

When the laser beam is scanned by galvo mirrors, the melt pool morphology in the transverse cross section remains nearly symmetric. However, in the longitudinal cross section, the symmetry is broken, as there is always a tail at the end of the pool (Matsunawa *et al.*, 1998; Parab *et al.*, 2018). Solid metal is absorbed by an advancing melt ahead of the beam, and the melt solidifies behind it. Under steady-state laser scanning on the sample surface, both the melting and solidification rates are equal to the scan velocity (Boettinger *et al.*, 1984; Kurz, Giovanola, and Trivedi, 1986). At low applied energy density (i.e., power divided by scan velocity), the melt pool is small, shallow, and more rounded (King *et al.*, 2014; Scipioni Bertoli, Wolfer *et al.*, 2017). With increasing energy density, the pool becomes deeper and larger and the surface starts to vaporize and deform, thereby creating a vapor depression with asymmetric morphology on the longitudinal cross section (Cunningham *et al.*, 2019). The front wall of the vapor depression is tilted, and its angle can be determined by the drill rate and scan velocity of the laser (Fabbro and Chouf, 2000; Cunningham *et al.*, 2019). Generally, the laser beam impinges mostly on this front wall, producing overheating and a strong vapor ejection along its normal and against the scan direction (Kaplan, 1994; Zhao *et al.*, 2019). However, at high applied energy density (as in the case of high laser power and low scan velocity), a deep and narrow vapor cavity instigates downward multiple reflections of the light (Kaplan, 1994; Cho and Na, 2006; Tan, Bailey, and Shin, 2013), leading to maximal temperatures at its bottom. This causes upward vapor ejection, which can resemble the stationary laser-beam case (Bidare *et al.*, 2018; Cunningham *et al.*, 2019).

C. Protrusion and keyhole instability

In both stationary and scanning cases, when the laser heating intensifies by increasing the power or dwell time (interaction time or laser spot size divided by scan velocity) of the laser beam, the resulting deep keyhole can lead to instability. The consequences are mainly twofold, as illustrated in Fig. 2(a). Above the sample surface, the vapor ejection shows chaotic behavior and some extremely fast spatters may be observed (Bidare *et al.*, 2018; Zhao *et al.*, 2019). Inside the sample, bubbles generated from the keyhole bottom tip can be accelerated by acoustic waves or viscous drag, and thus potentially captured by the advancing solidification front as pore defects (Zhao *et al.*, 2017, 2020, 2022; Bayat *et al.*, 2019; Kiss *et al.*, 2019). The keyhole pores are either vacuum or gas filled after complete condensation depending on the processing environment and powder conditions (Weingarten *et al.*, 2015; Cunningham *et al.*, 2016; Kosonen, Kakko, and Raitanen, 2021; Huang *et al.*, 2022).

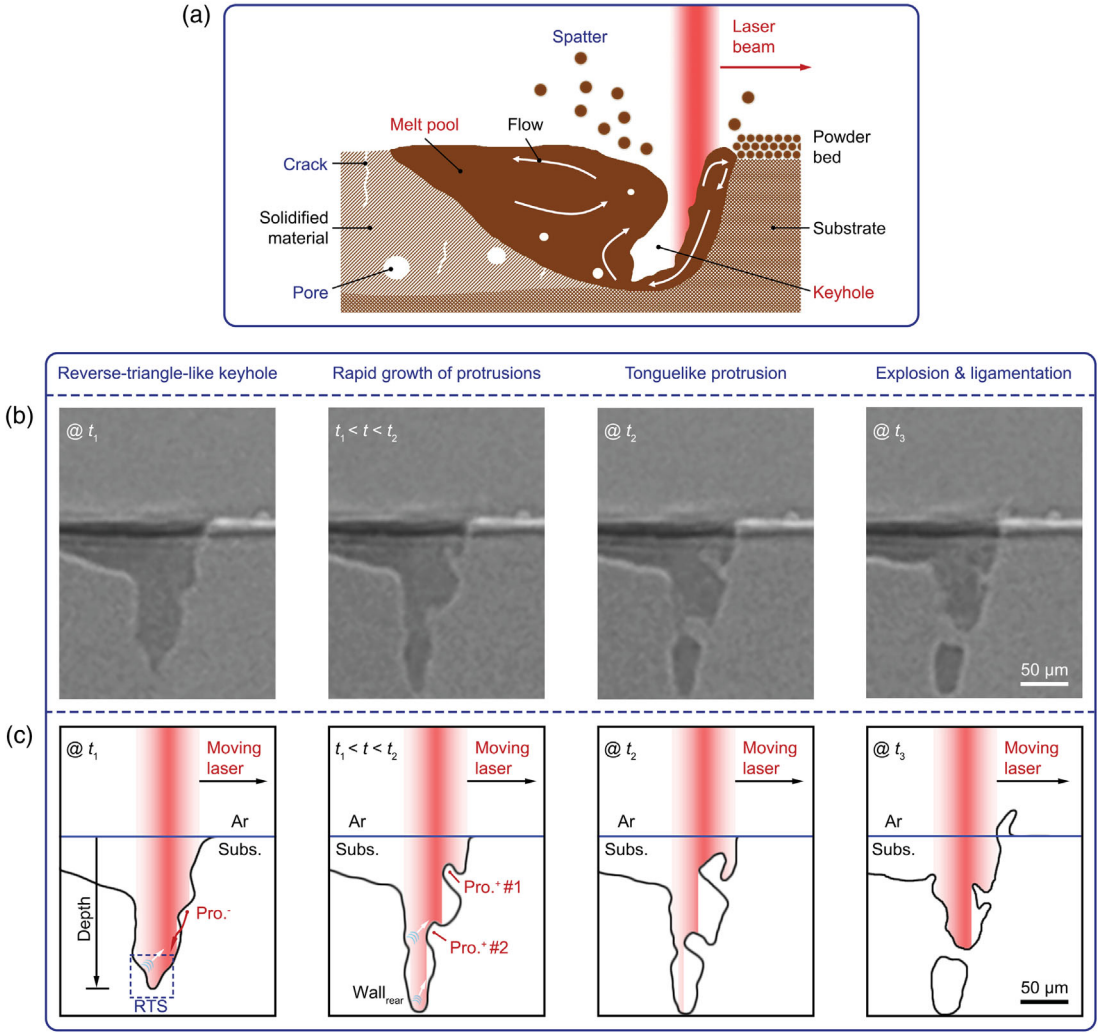

FIG. 2. Melt pool, keyhole, and common defects in unstable-keyhole-mode melting. (a) Schematic showing the general melt pool structure. The white arrows inside the melt pool indicate the flow pattern of the melt. (b),(c) Protrusion structure on the front wall of an unstable keyhole. (b) High-speed, high-energy x-ray images. (c) Schematic illustrations. At time t_1, a keyhole of reverse-triangle-like shape (RTS) forms. The rear wall is directly exposed to the incident laser beam, and the generated vapor then travels upward toward the front wall, as indicated by the blue arc lines and white arrows in (c). Upon the collision with the vapor, the existing protrusions (such as Pro. #1 and Pro. #2) change from a dome shape leaning downward (denoted by Pro^-) to a rod shape tilting upward (denoted by Pro^+). Here the rapid growth and collapse of the tonguelike protrusion Pro. #1 eventually leads to the formation of extremely fast ligaments and spatters, and the collapse of protrusion Pro. #2 causes the formation of an instant keyhole pore. (b),(c) Adapted from Zhao *et al.*, 2019.

They differentiate from the gas entrainment pores that are caused by the environmental gas being trapped into the melt pool, which does not necessarily involve a highly unstable keyhole (Martin *et al.*, 2019b; Hojjatzadeh *et al.*, 2020).

The extremely fast spatters and keyhole pores are directly related to a structure on the front keyhole wall called protrusion (Zhao *et al.*, 2019, 2020). For example, in Figs. 2(b) and 2(c), under a scanning continuous-wave laser beam the solid phase ahead of the front keyhole rim is heated, melted, and vaporized, forming a small vapor depression and a dome-shaped protrusion (Zhao *et al.*, 2019). This protrusion, propelled by the recoil momentum from the intense vaporization of its top surface layer ($10^5 - 10^6$ Pa, orders of magnitude higher than the capillary and thermocapillary forces) (Kroos, Gratzke, and Simon, 1993; Lee *et al.*, 2002; Tan, Bailey, and Shin, 2013; Kouraytem *et al.*, 2019), flows down along the front keyhole wall. Through statistical analysis of the protrusion speed, the average temperature on the front wall can be estimated to reach hundreds of kelvins above the boiling point (Anisimov and Khokhlov, 1995; Semak and Matsunawa, 1997). Under certain laser irradiation conditions, the keyhole bottom becomes a reverse-triangle-like (or inverted-triangle-like) shape. A following protrusion (Pro. #1) appears at the front wall rim and flows downward. During the downflow process, the bottom surface of the protrusion is believed to be supported by the directional collision of the vapor that is strongly ejected from the bottom of the rear wall, causing a shape change from a dome leaning downward to a rod tilting upward. The protrusion then appears to stop running down and rest for a while. Meanwhile, with the scanning of the beam new melt forms, flows down, and merges into Pro. #1. As a result, the protrusion grows rapidly and becomes tonguelike in shape with a minikeyhole on its top. Eventually, the protrusion

explodes because of irregular internal thermal and pressure fluctuations and causes the ejections of melt ligaments and fast spatters (>40 m/s in the case of a Ti-6Al-4V alloy).

D. Limitations

The extreme thermal conditions in laser melting create many highly dynamic physical phenomena. A thorough understanding of them is essential for the ability to tailor microstructures and eliminate defects (Gu and Shen, 2007; Islam *et al.*, 2013; Cunningham, Narra *et al.*, 2017; Zhao *et al.*, 2019, 2020; Pollock, Clarke, and Babu, 2020; Thampy *et al.*, 2020; Todaro *et al.*, 2020; Martin *et al.*, 2021). However, they are too detailed and are overly complex for routine process development. In reality, their collective effects, the melt pool and vapor depression morphologies, are used as the guideline (Paul and Debroy, 1988; Assuncao, Williams, and Yapp, 2012; King *et al.*, 2014; Qi *et al.*, 2017; Simonds *et al.*, 2018; Cunningham *et al.*, 2019). They define the melting modes, as we now summarize.

III. POSTMORTEM- AND PROCESS-BASED MELTING MODES

The melting modes, as shown in Fig. 3(a), bridge laser-matter interactions and microstructures as well as defects. They ignore the physical details and focus on the macroscopic appearance of (fused) melt pool (and possibly also the vapor depression). According to measurement methods, the modes can be postmortem or process based. For the postmortem-based definitions, the morphology of melt pool is derived from the postmortem transverse cross section (Paul and Debroy, 1988; Assuncao, Williams, and Yapp, 2012; King *et al.*, 2014; Qi *et al.*, 2017; Scipioni Bertoli, Wolfer *et al.*, 2017; Simonds *et al.*, 2018). In the process-based version, the morphologies of the melt pool and vapor depression are measured directly from the *in situ* and real-time data (including high-speed x-ray images) (Cunningham *et al.*, 2019; Chen *et al.*, 2020; Zhao *et al.*, 2020). With increasing temperature, the aspect ratio of the (fused) melt pool (and possibly also the vapor depression) in either case increases. Accordingly, the melting mode changes from conduction (via the transition) to keyhole.

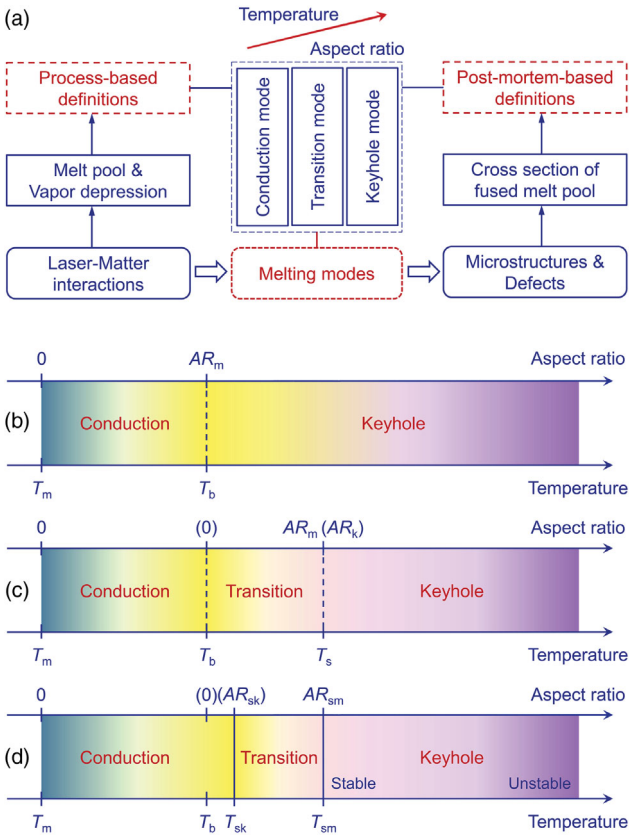

FIG. 3. Postmortem-based and process-based definitions of laser melting modes. (a) Basis for definitions. With increasing temperature the depth-to-width aspect ratio of the (fused) melt pool (and possibly also the vapor depression) increases, and the laser melting transitions from conduction to keyhole mode. (b)–(d) Historical evolution of the definitions. (b) Original and (c) updated versions of postmortem-based definitions. (d) Process-based definitions. Along the axis of aspect ratio (AR), the values in brackets are the characteristic aspect ratios of the vapor depression; otherwise, they are the characteristic aspect ratios of the (fused) melt pool. The AR_k at T_s in (c) and AR_{sk} at T_{sk} in (d) are aspect ratios where the vapor depression starts to deviate from the semicircular shape. The AR_m at T_s in (c) and AR_{sm} at T_{sm} in (d) are aspect ratios where the (fused) melt pool starts to deviate from the nearly semicircular shape.

A. Postmortem-based definitions

Traditionally, the melting modes have been defined based on mainly practical and partially theoretical evidence (Dowden, Davis, and Kapadia, 1985; Kaplan, 1994; Semak and Matsunawa, 1997; Rai *et al.*, 2007; King *et al.*, 2014; Scipioni Bertoli, Wolfer *et al.*, 2017). Because of the lack of effective tools to characterize the transient nature of the subsurface melt pool and vapor depression, our understanding of laser melting has relied heavily on subjective experience and simulation modeling for decades.

1. Theoretical consideration

In theory, the characteristic temperature points appear as ideal thresholds that separate the melting modes, as illustrated in Figs. 3(b) and 3(c). Originally, only the boiling point (T_b) or a point below the boiling (T_c) was used [Fig. 3(b)] (Dowden, Davis, and Kapadia, 1985; Semak and Matsunawa, 1997; Zhao and DebRoy, 2003; Rai *et al.*, 2007; King *et al.*, 2014; Scipioni Bertoli, Wolfer *et al.*, 2017; Fabbro *et al.*, 2018). Below T_b or T_c, the melting is in the conduction mode and conductive heat transfer largely governs the melt pool geometry (Eagar and Tsai, 1983; Kaplan, 1994; Shu *et al.*, 2021; Derimow *et al.*, 2022), while above the point it is in keyhole mode and the melt pool morphology is controlled mainly by convective heat transfer (Semak and Matsunawa, 1997; Rai *et al.*, 2007; Bauereiß, Scharowsky, and Körner, 2014; Khairallah *et al.*, 2016). This intuition captures some features of the melt pool. For example, once the applied energy density is above a threshold, the melt pool grows rapidly in depth (King *et al.*, 2014). However, the role of vaporization (initially at least) has been greatly exaggerated. Upon boiling, the recoil pressure from the vaporization is in fact insufficient to power

the fast growth of the vapor depression or the melt pool (Cunningham *et al.*, 2019; Wang, Zhang, and Yan, 2020). Later a second characteristic temperature T_s was introduced, and it is the point at which the recoil pressure starts to overcome the surface tension pressure [Fig. 3(c)] (Hirano, Fabbro, and Muller, 2011; Trapp *et al.*, 2017). That is, between the two modes there is a transition mode in which conductive and convective heat transfers compete (Lee *et al.*, 2002; Assuncao, Williams, and Yapp, 2012). This update closes several loopholes in the original definitions, such as the occurrence of rapid vaporization prior to the keyhole mode, and the results seem to match the experimental observations [Figs. 4(b) and 4(c)]. We point out that heat convection cannot be ignored in the conduction mode to accurately describe the melt pool morphology (Shu *et al.*, 2021; Derimow *et al.*, 2022).

2. Traditional definitions

In practice, these two or three melting modes (conduction, transition, and keyhole) are often defined according to the postmortem transverse cross section of a fused melt pool (Paul and Debroy, 1988; Assuncao, Williams, and Yapp, 2012; King *et al.*, 2014; Qi *et al.*, 2017; Scipioni Bertoli, Wolfer *et al.*, 2017; Patel and Vlasea, 2020). For example, in Fig. 4(a), when it is shallow, semicircular, and has a low aspect ratio (i.e., a subsurface depth to width), the melting is considered to be in the conduction mode; when it is deep and conical and has a high aspect ratio, the melting is in the keyhole mode (King *et al.*, 2014; Scipioni Bertoli, Wolfer *et al.*, 2017). In the transition mode, the cross section is in between and may combine the two shapes (Assuncao, Williams, and Yapp, 2012; Qi *et al.*, 2017; Simonds *et al.*, 2018). Figure 4(b) shows the relationship between the melting mode and the scan velocity (Qi *et al.*, 2017). Under a scanning laser beam with constant power and spot size, as the velocity increases the mode shifts from keyhole to transition to conduction. Similarly, Fig. 4(c) describes the melting mode transitions for a stationary laser beam (Assuncao, Williams, and Yapp, 2012). For the same spot size and interaction time, with the increase in laser irradiance (also known as the power density, the laser power divided by the area), the aspect ratio of the cross section in the transition mode is characterized by a plateau.

These postmortem-based definitions are simple and conceptually reasonable. They have served as guidelines to the community for decades: in metal AM, the so-called conduction mode or the beginning of the transition mode is used here to avoid excessive porosity (DebRoy *et al.*, 2018). Compared to the original ones, the updated definitions represent an improvement. However, there are no clear boundaries that separate the three modes, and the value of the plateau in Fig. 4(c) varies with laser spot size and interaction time. The postmortem-based definitions have historic limitations because of the lack of direct observation of melt pool and vapor depression dynamics (such as morphology evolutions).

B. Process-based definitions

1. Conceptual definitions

The *operando* high-speed synchrotron x-ray imaging technique was first reported by Zhao *et al.* (2017) to monitor the laser fusion AM process (see the Appendix for

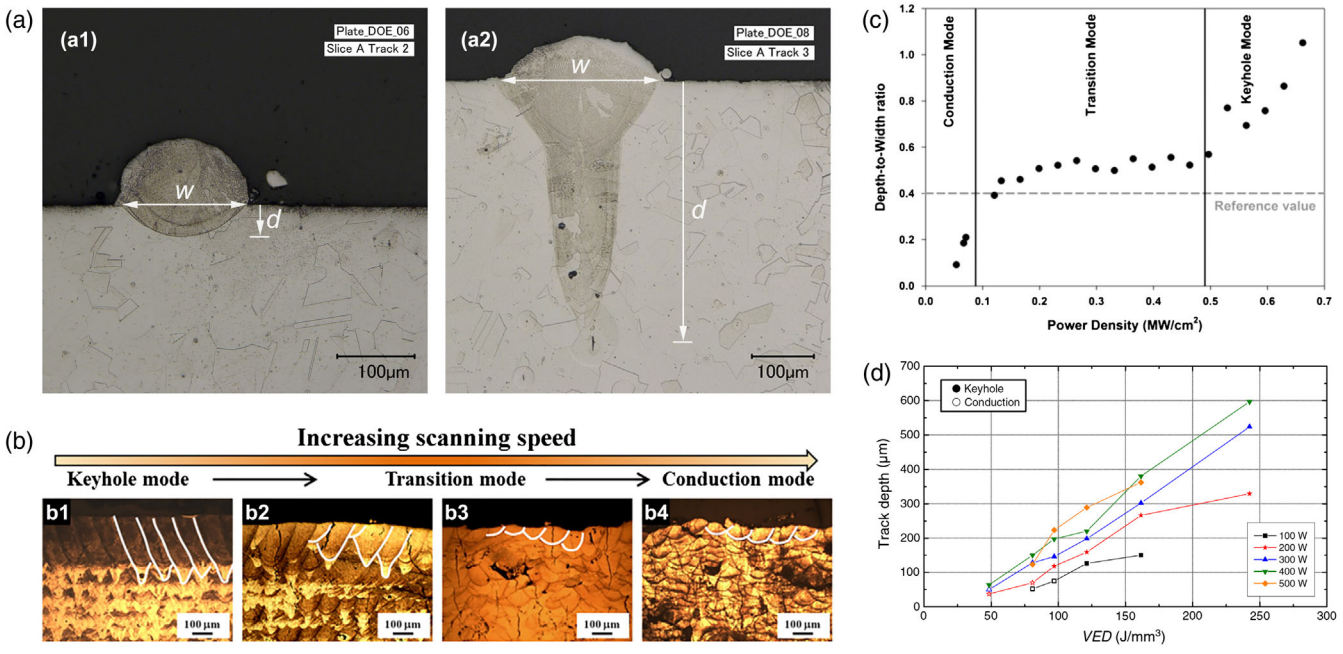

FIG. 4. Laser melting modes defined by postmortem transverse cross sections of the fused melt pool. (a) Original definitions of (a1) conduction mode and (a2) keyhole mode. The depth d and width w to calculate the aspect ratio are marked in white. From King *et al.* (2014). (b) Melting mode transitions via varying scan velocity in laser powder bed fusion. From Qi *et al.* (2017). (c) Aspect ratio of the fused melt pool as a function of power density. The laser is a stationary beam, and the spot size and the interaction time are constants. From Assuncao, Williams, and Yapp (2012). (d) Depth of the fused melt pool as a function of volumetric energy density. From Scipioni Bertoli, Wolfer *et al.* (2017).

TABLE I. Melting modes defined by high-speed x-ray imaging of stationary laser melting.

Melting modes	Vapor depression transition	Melt pool transition	
	Conduction mode	Transition mode	Keyhole mode
Vapor depression	May exist If it exists, it is shallow and semicircular Stable	Deep and conical Fluctuation	May show strong fluctuation and collapse
Melt pool	Shallow and semicircular Stable and almost synchronized with the vapor depression.	Semicircular Stable	Deep and conical or bimodal (a bowl on the top and a spike at the bottom) Weak fluctuation

additional details). With unprecedented temporal and spatial resolutions as well as high frame rates (subnanosecond, micrometer, and megahertz) that are orders of magnitude higher than those in laboratory x-ray imaging (Matsunawa *et al.*, 1998), the highly dynamic and transient physical processes, particularly the melt pool and vapor depression behavior below the sample surface, have been probed (Zhao *et al.*, 2017, 2019, 2022; Calta *et al.*, 2018; Leung *et al.*, 2018; Miyagi *et al.*, 2018; Parab *et al.*, 2018; Martin *et al.*, 2019a; Wolff *et al.*, 2019; Hocine *et al.*, 2020). And as a result the definitions of laser melting modes have been revised accordingly (Cunningham *et al.*, 2019). The results are summarized in Table I and Figs. 5(a)–5(c). Under a stationary laser beam, the melting mode changes over time from conduction to transition to keyhole.

In the conduction mode, the melt pool is stable and shows a quasisemicircular morphology. This is consistent with traditional postmortem cross-section results (Assuncao, Williams, and Yapp, 2012; King *et al.*, 2014; Qi *et al.*, 2017; Scipioni Bertoli, Wolfer *et al.*, 2017). However, a shallow and semicircular vapor cavity may exist inside the melt pool because of the high irradiance at the center of a Gaussian profiled laser beam (Cunningham *et al.*, 2019; Wang, Zhang, and Yan, 2020; Wei *et al.*, 2022). This is different from pure conduction. As shown in Fig. 3(c), in the updated postmortem-based definitions strong vaporization begins in transition mode. Meanwhile, in the definitions described here [Fig. 3(d)] the end point of the conduction mode lies beyond the boiling point.

In the transition mode, the melt pool maintains a stable and quasisemicircular shape, while the vapor depression becomes deep and conical and exhibits fluctuations. This detailed information was missing from prior reports (Lee *et al.*, 2002; Assuncao, Williams, and Yapp, 2012; Qi *et al.*, 2017; Tenbrock *et al.*, 2020). In our traditional understanding, it is believed that the evolutions of the melt pool and vapor depression morphologies are synchronized or that they are both quasisemicircular (Trapp *et al.*, 2017). But here the vapor depression dynamics are much more transient than the melt pool dynamics. In Fig. 3(d), the temperature point at which the recoil pressure starts to overcome the surface tension pressure is denoted by T_{sk} instead of T_s. It is the beginning of the transition mode, not yet the keyhole mode.

In the keyhole mode, the melt pool is deep and narrow and may show a bimodal shape with a bowl on the top and a spike at the bottom. This is largely consistent with traditional results. The differences are twofold. On the one hand, the vapor depression, compared to the melt pool, may exhibit much stronger fluctuations (i.e., a larger amplitude and a higher frequency); on the other hand, in Fig. 3(d) the temperature point at which the melt pool starts to grow rapidly in the depth direction is written as T_{sm}, which is similar but not necessarily identical to the T_s quantity in the postmortem-based definitions. In addition, the keyhole mode regime is subdivided into stable- and unstable-keyhole regions. In the unstable region, the instability of the vapor depression (i.e., strong fluctuation and collapse) could cause spatter ejection and pore formation (Matsunawa *et al.*, 1998; Khairallah *et al.*, 2016; Zhao *et al.*, 2017, 2019, 2020; Kiss *et al.*, 2019; Khairallah *et al.*, 2020).

A vapor depression could exist in all three melting modes. That is, the laser beam generally does not interact with a flat melt pool directly, but instead through some sort of vapor depression, either shallow or deep.

From the perspective of thermal transport, the two temperature points T_{sk} and T_{sm} depend mainly on local absorbed laser energy, melt flow flux, thermal diffusion flux, evaporation latent heat, solid-liquid transition latent heat, and heat loss from surface radiation and convection (Ki, Mazumder, and Mohanty, 2002; Cook and Murphy, 2020). Given a Gaussian beam, a material, and a processing environment, when there is an abrupt increase in laser absorption because of light trapping and focusing and thus in temperature and recoil pressure at the bottom of the vapor depression, the force balance on the local vapor-liquid interface is broken (Wang, Zhang, and Yan, 2020; Wei *et al.*, 2022). The vapor depression then becomes unstable and grows rapidly in depth, with a conical tip [Fig. 5(b)]. As the tip is close to the melt pool bottom, the large local thermal gradient causes a high Marangoni force and thus a violent melt flow. This transports a large amount of heat to the solid-liquid interface of the melt pool bottom, beyond the thermal regulation capacity. As a result, the melt pool becomes unstable and shows a conical or spike tip [Fig. 5(c)].

Based on the morphologies of both the melt pool and the vapor depression, the melting modes have been redefined (Cunningham *et al.*, 2019). Although the example in Fig. 5(c) uses a stationary laser beam, the approach can be extended to the scanning laser case either by converting the transition times to the critical scan velocities [Fig. 5(f)] or by

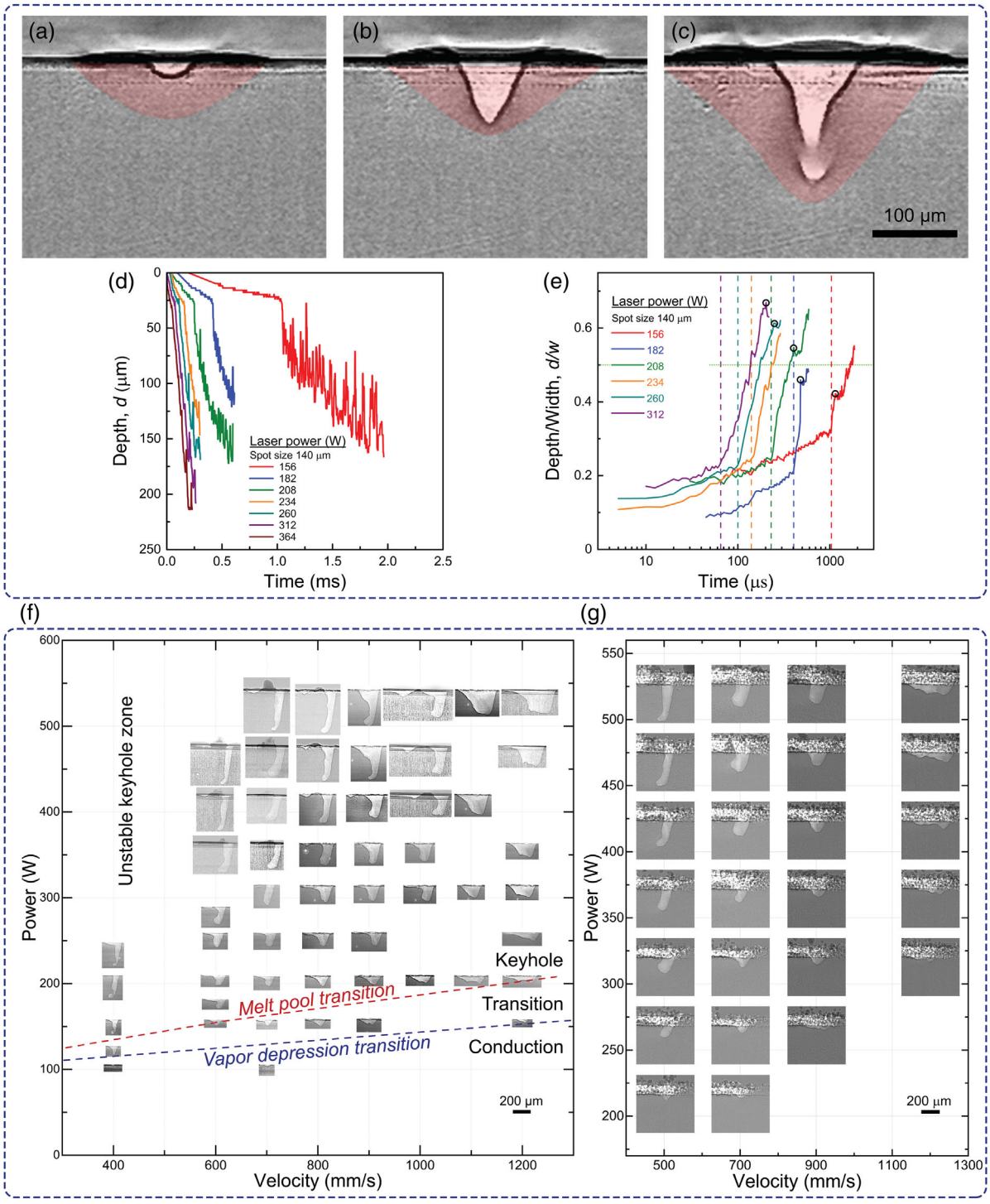

FIG. 5. Laser melting modes defined by the vapor depression and melt pool morphologies through high-speed synchrotron x-ray imaging. (a)–(c) Conceptual definitions in stationary laser melting. From left to right, conduction, transition, and keyhole modes are displayed. The light area is the vapor depression and the red shaded area shows the melt pool. (d),(e) Strict definitions based on a quantitative morphology measurement from (a)–(c). (d) Penetration depth of vapor depression and (e) the aspect ratio of the melt pool over time at various laser powers. The transitions in (d) and the time points indicated by the vertical dashed lines in (e) define the vapor depression transition. The open circles in (e) define the melt pool transition. (f),(g) Extended definitions in the P-V space for the case of a scanning laser. (f) Bare plate. (g) Powder bed. The lower blue and upper red dashed lines in (f) outline the vapor depression and melt pool transitions, respectively. The laser spot size in (f) is 95 μm, and that in (g) is 115 μm. Adapted from Cunningham *et al.*, 2019.

examining the transverse cross sections of the melt pool and the vapor depression. These process-based definitions break the historic limitations and offer new community guidelines. Most of all, to a large extent it is the vapor depression that bridges the laser beam and the melt pool in laser fusion AM of metals.

2. Strict definitions

The term keyhole needs to be reconsidered prior to the strict definitions of melting modes. Rather than an empirical derivation from the traditional postmortem transverse cross section of a fused melt pool, we prefer to redefine it directly from the morphology of the vapor-dominated cavity. When the cavity deviates from the semicircular shape, it is a keyhole. Strictly speaking, we propose that for a cavity with the width w, if some portion of the incident laser beam at a location less than $w/4$ away from the laser-beam centerline reflects more than once inside the cavity, it is a keyhole. Ray tracing, where the laser beam is represented by a collection of idealized narrow beams called rays, is a geometrical approach to calculating laser propagation and absorption (Boley, Khairallah, and Rubenchik, 2015; Zhao *et al.*, 2019). In the strict keyhole definition proposed here, angle- and polarization-dependent absorptivity is not considered.

Under a stationary laser beam with a given spot size, the melting mode depends on both the laser irradiance and the interaction time (Assuncao, Williams, and Yapp, 2012; Cunningham *et al.*, 2019). To strictly define the modes, some aspects of the physical process of laser melting (i.e., vapor depression and melt pool evolutions) are needed. That is, the interaction time, not the irradiance, is demonstrated here.

In Fig. 5(d), for a given laser power and spot size the curve of the vapor depression depth versus time shows a distinct transition point, before which the depth grows slowly at a nearly constant rate and after which the depth starts to fluctuate. The transition at this time point is defined as the vapor depression transition. It strictly defines the upper limit of the conduction mode and the lower limit of the transition mode (Table I). Before the transition, the cavity is not a keyhole in the strict sense.

In Fig. 5(e), the depth-to-width aspect ratio of the melt pool over time exhibits two distinct transitions. The first transition coincides with the vapor depression transition defined in Fig. 5(d), after which the aspect ratio increases rapidly. This coincidence indicates that the vapor depression dynamics in the conduction mode, if there is a vapor cavity, is relatively slow and the melt pool dynamics can catch up. The second transition occurs when the aspect ratio reaches a value of about 0.5 (varies with laser power), after which the increase in aspect ratio stagnates. This transition is defined as the melt pool transition, which defines the upper limit of the transition mode and the lower limit of the keyhole mode (Table I).

Here two transition times are involved: one is the time to the vapor depression transition and the other is the time to the melt pool transition. Both decrease rapidly with the increase in laser irradiance. This could be the physical foundation of melting modes in the laser power-scan velocity space. We note that, as indicated in Fig. 5(e), the aspect ratio of the melt pool for the second transition is not constant but instead positively related to the irradiance. That is why in Fig. 3(d) we state that the temperature point of T_{sm} (or the aspect ratio value of AR_{sm}) does not equal the point of T_s (or the value of AR_m) in the traditional definitions.

3. From stationary to scanning

For a given spot size, the two main processing parameters for a scanning laser beam are laser power (P) and velocity (V). They constitute the P-V space (Ion, Shercliff, and Ashby, 1992; Kruth *et al.*, 2005; Beuth *et al.*, 2013; Gong *et al.*, 2014; Cunningham *et al.*, 2019; Scime and Beuth, 2019b; Zhao *et al.*, 2020). It is an effective but heuristic approach in laser fusion additive manufacturing to directly relate the build quality to the P-V space. In comparison to other studies that used the density or porosity or fused melt pool or mechanical strength that is postmortem based as the metric, Figs. 5(f) and 5(g) use a transient vapor depression that is process based. When the velocity approaches zero, the scanning beam becomes stationary. In other words, on the macro level, regardless of their differences (such as asymmetric melt pool and vapor depression morphologies under scanning), the stationary and scanning beams are intrinsically connected via the laser-matter interaction time (Cunningham *et al.*, 2019; Zhao *et al.*, 2020).

As mentioned, the melting modes defined under a stationary beam could be extended to the scanning case through the two transition time points t_d and $V_d = D/t_d$, where D is the laser spot size. For a given laser power, there are two critical velocity points corresponding to the vapor depression and melt pool transitions, respectively. For a series of powers, these points could be connected to two lines, dividing the P-V space into conduction, transition, and keyhole regimes. In Fig. 5(f), the lower blue line is for the vapor depression transition and the upper red line is for the melt pool transition. Additionally, the keyhole regime could be further classified into stable and unstable regions, with the latter corresponding to the high-power and low-velocity areas in the P-V space.

As for the role of powder in laser powder bed fusion AM, note that the stable-keyhole morphology (as well as the melting mode) follows the same trend regardless of the presence of powder [Figs. 5(f) and 5(g)] (Cunningham *et al.*, 2019). This accords with the general observation that the presence of powder makes little difference to the melt pool size. Teams at the Lawrence Livermore National Laboratory and the University of California, Santa Barbara, claimed that the details of the powder become far less important when the power is above a certain value (Khairallah *et al.*, 2020; Polonsky and Pollock, 2020). More recently the role of powder around the keyhole porosity regime was statistically analyzed. The results show that the addition of powder increases the keyhole instability but widens the porosity regime in the P-V space only slightly (Zhao *et al.*, 2020). An additional effect of the powder is that the gas atomized powder typically contains porosity, a fraction of which may be inherited (Aboulkhair *et al.*, 2014; Cunningham, Nicolas *et al.*, 2017; Iebba *et al.*, 2017).

According to the extended definitions in Figs. 5(f) and 5(g), nearly all the P-V combinations, including those commonly used in commercial laser powder bed fusion AM machines, are in the transition or keyhole mode. This is surprising. To some extent, it shows why it is always extremely challenging to eliminate keyhole pores (not formed at laser turn points or caused by imperfect powder spreading) when the machines

are operated in the supposed conduction mode (Cunningham, Narra *et al.*, 2017; Martin *et al.*, 2019b; Zhao *et al.*, 2020).

These extended definitions of melting modes in the *P-V* space are not strict, particularly in the low-power and low-velocity region where the vapor depression and melt pool fluctuations are significant. They are simply derived from the stationary laser measurements and are good for basic evaluations. This is consistent with the fact that the applied energy density parameter has limitations for precise quantification of the melt pool depth as well as the melting mode [Fig. 4(d)] (Prashanth *et al.*, 2017; Scipioni Bertoli, Wolfer *et al.*, 2017). This may be attributed to the large variation in the vapor depression morphology across the space [Figs. 5(f) and 5(g)], which can significantly alter the laser absorption through multiple angle-dependent absorption events. This in turn affects the melt flow hydrodynamics through Marangoni convection, recoil pressure, and vapor impact, and ultimately also the melt pool morphology (Kouraytem *et al.*, 2019).

In practice, the melting modes under a scanning laser beam can be defined according to the transverse cross sections of the melt pool and the vapor depression. This may be assisted by the three-dimensional multiphysics simulations after model calibration and validation using high-speed synchrotron x-ray imaging data (Kouraytem *et al.*, 2019; Khairallah *et al.*, 2020; Wang, Zhang, and Yan, 2020; Gan *et al.*, 2021; Wei *et al.*, 2022), which resembles those under a stationary beam [Figs. 5(a)–5(e) and Table I]. For example, when the vapor depression deviates from semicircular, the laser melting enters the transition mode. Under the low-power and low-scan-velocity laser conditions, the vapor depression may appear to be extremely narrow (much smaller than the laser spot size) and to have a high aspect ratio. The main reasons are threefold. First, the laser absorption increases because of multiple reflections. Second, the edge of the low-power Gaussian beam cannot provide sufficient energy to vaporize the metal. Third, the laser melting may transition from conduction to stable-keyhole to unstable-keyhole mode during a scan because of variations in local material or laser conditions such as sample preheating or surface oxidization ahead of the laser-beam or powder motion and shading above the surface (Rubenchik *et al.*, 2014; Yang *et al.*, 2018; Martin *et al.*, 2019a; Khairallah *et al.*, 2020; Zhao *et al.*, 2020).

IV. GAPS IN KNOWLEDGE AND OPPORTUNITIES

A. Emerging knowledge

A few key points of the process-based definitions are summarized here. First, there is the potential for the vapor depression formation in all three modes, and beyond the conduction mode the vapor depression dynamics are much more transient than the melt pool dynamics. Second, under stationary laser melting the two time nodes corresponding to the vapor depression and melt pool transitions strictly define the three melting modes. Third, the melting modes in the stationary laser melting could be extended to the scanning case, according to which commercial AM machines are typically operated in either the transition or the stable-keyhole mode. However, as in the case using applied energy density as a measure, caution should be exercised because of the large variations in the vapor depression morphology and laser absorption across the *P-V* space. Alternatively, the modes under a scanning beam could be defined by the transverse cross sections of the melt pool and the vapor depression. The multiphysics simulations after model calibration and validation play an essential role in connecting the longitudinal and transverse cross sections of the vapor depression and the melt pool, as well as deriving the process-based definitions from the postmortem evidence by providing three-dimensional structure information (Rai *et al.*, 2007; Kouraytem *et al.*, 2019; Khairallah *et al.*, 2020; Wang, Zhang, and Yan, 2020; Gan *et al.*, 2021; Wei *et al.*, 2022).

B. Beyond x-ray imaging

Operando high-speed synchrotron x-ray imaging has been an invaluable tool for probing the laser fusion process. In addition to direct measurement, the melt pool and vapor depression morphology evolutions could be translated into other signal forms such as dynamic laser absorption, vapor plume dynamics, and ultrasound signals for the mode definitions through (as shown in Fig. 6) a combination of high-speed x-ray imaging and other *in situ* and real-time monitoring techniques, such as integrating sphere radiometry (Khairallah, Sun, and Simonds, 2021; Simonds *et al.*, 2021), schlieren imaging (Bidare *et al.*, 2018; Bitharas *et al.*, 2022), and immersion ultrasound (Gillespie *et al.*, 2021). These could be feasible and efficient approaches for process monitoring where in-process x-ray imaging is not an option (Zhao *et al.*, 2022). To facilitate the translations (also between the *in situ* and *ex situ* data), physics-based modeling, the big data

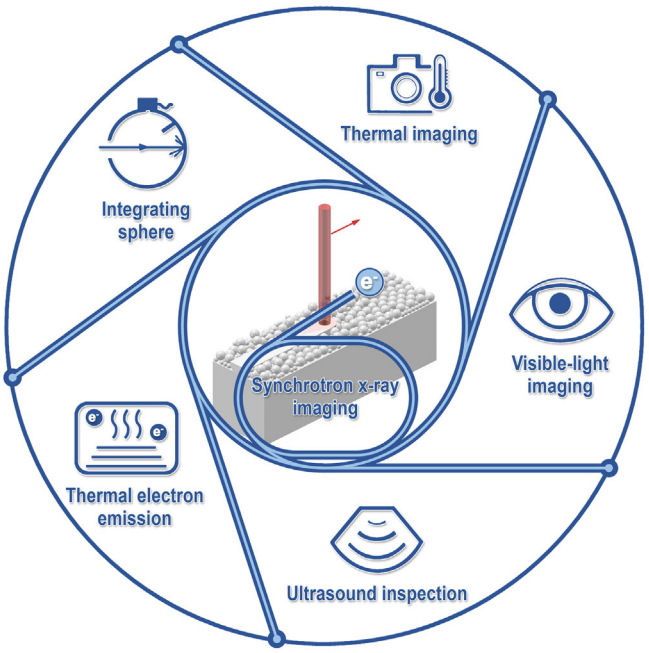

FIG. 6. Integration of *operando* synchrotron x-ray imaging and other high-speed *in situ* monitoring techniques. Through multitechnique fusion and multisignal translation, the emerging knowledge obtained from synchrotron x rays can be transferred to industrial practice.

approach, and appropriate experimental design are the key (Scime and Beuth, 2019b; Shevchik *et al.*, 2019; Zhang, Liu, and Shin, 2019; Gan *et al.*, 2021; Zhu, Liu, and Yan, 2021).

For example, a team at the National Institute of Standards and Technology combined integrating sphere radiometry and high-speed x-ray imaging and correlated the laser absorption with the vapor depression evolution and melting modes (Simonds *et al.*, 2021). The energy absorbed by the sample during the laser melting process is calculated from the energy balance of the incident light and the absolute reflected light measured by the spheres (Fabbro *et al.*, 2006; Norris and Robino, 2008). The energy absorption increases sharply when the laser melting enters into the transition mode from the conduction mode, drops upon the decrease of the vapor depression depth (Simonds *et al.*, 2021), and periodically fluctuates when the probability of forming a transient keyhole pore increases (Simonds *et al.*, 2020; Khairallah, Sun, and Simonds, 2021). These correlations along with the high temporal resolution and readily processable one-dimensional data stream make absolute absorption an appealing approach for process-based melt pool monitoring.

Immersion ultrasound was also performed simultaneously with high-speed x-ray imaging to monitor the melt pool and vapor depression dynamics (Gillespie *et al.*, 2021). The basic principle of the ultrasound technique is that the amplitude of the scattered waveform is a result of local variations in elastic properties and mass density (Schmerr, 2016; Shevchik *et al.*, 2018). In this study, the time of flight of the ultrasound scattering from the melt pool was found to be highly sensitive to the depth of the melt pool (Gillespie *et al.*, 2021). This technique could in principle be implemented in the industrial-scale additive manufacturing process. However, more research effort is needed because of the complex nature of the ultrasonic signal itself.

C. Stable-keyhole AM

These process-based definitions offer new guidelines to the AM community. One direct conclusion is that, in the laser powder bed fusion AM of metals, a stable-keyhole region is desirable to achieve full-density builds. The transition region is much smaller than the stable-keyhole region. Together they outline the process window for a metallic material, as illustrated in Fig. 7(a). Outside of the window, the *P*-*V* space is occupied by several zones that potentially create microstructural defects or dimensional inaccuracy, among them keyhole porosity, balling, and lack-of-fusion porosity (Chandrasekhar, 1981; Tolochko *et al.*, 2004; Gu and Shen, 2007; Amara and Fabbro, 2010; Tang, Pistorius, and Beuth, 2017; DebRoy *et al.*, 2018, 2021; Scime and Beuth, 2019b;

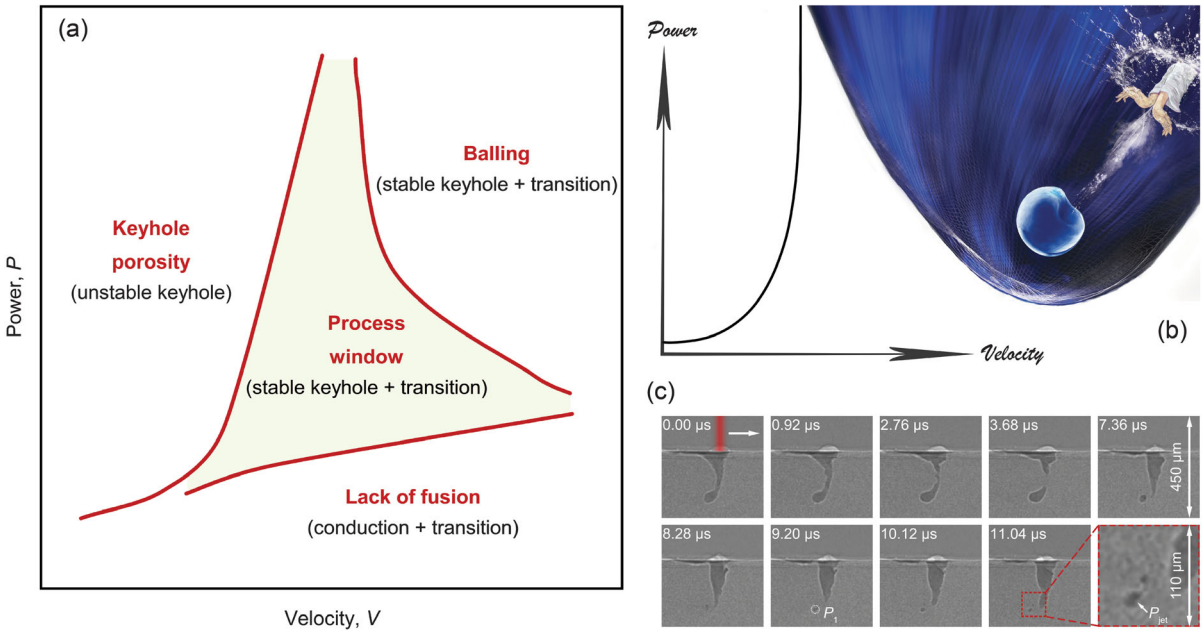

FIG. 7. Schematic diagrams of a process map for the laser powder bed fusion of metals. (a) Process window. The process window is located at the center of the *P*-*V* space and is surrounded by several common defect zones. The definitions of melting modes here are process based. Only part of the mixing stable-keyhole and transition region constitutes the window. At low energy density (low power and high scan velocity), balling can extend the region of lack-of-fusion porosity by causing variability in the melt pool size, and thus, the overlapping area between the "balling" and "lack-of-fusion" regions is designated as the latter. (b),(c) Boundary and origin of keyhole porosity. (b) Keyhole porosity boundary and origin. On the left side, the keyhole porosity boundary in the *P*-*V* space is sharp and smooth. On the right side, around the porosity boundary the critical keyhole instability that is analogous to a double palm strike emits an acoustic wave (shock wave) and drives the pore near the keyhole tip to accelerate rapidly away from the keyhole. When the pore is captured by the solidification front, it becomes a detrimental structural defect in the build. (c) X-ray images of keyhole pore formation and motion around the keyhole porosity boundary. In the first few microseconds after a pore pinches off the keyhole, the original keyhole tip remains nearly stationary. The pore P_1 marked with a dashed circle is then accelerated to about 10 m/s in less than 1 μs. At the time 11.04 μs, a microjet P_{jet} (see the inset) is penetrating into the pore P_1 from the side facing the keyhole bottom. The x-ray images are background corrected and the contrast is then reversed to highlight the events around the keyhole. (c) Adapted from Zhao *et al.*, 2020.

Snow, Nassar, and Reutzel, 2020; Zhao *et al.*, 2020; Gan *et al.*, 2021; Laleh *et al.*, 2021; Sanaei and Fatemi, 2021; Zhu *et al.*, 2021; Huang *et al.*, 2022; Mostafaei *et al.*, 2022). To take full advantage of this window, we need to confirm and understand its boundaries. In practice, these boundaries are often approached as process engineers strive to increase build rates or as local variations in build conditions (such as laser spot size, scan velocity, air flow, and powder bed surface) create momentary deviations from prescribed *P*-*V* parameters. In other words, there is a need to uncover the fundamental origins of those defects. As an example, in Figs. 7(b) and 7(c) (Zhao *et al.*, 2020) it is discovered through high-speed synchrotron x-ray imaging that the keyhole porosity boundary is smooth and sharp. Only when pores near the keyhole tip obtain sufficient kinetic energy from the acoustic waves (high amplitude, short duration, and depth oriented) released from the critical keyhole instability (in analogy with a double palm strike in the artwork) can they escape rapidly from the large thermal gradient field around the keyhole and become trapped by the solidification front as defects. This acoustic-wave-driven mechanism is distinct from the viscous-drag-driven mechanism, which requires sufficient waiting time created by the retracting keyhole (Bayat *et al.*, 2019; Zhao *et al.*, 2020).

From another perspective, in comparison to conduction-mode AM, the stable-keyhole-mode AM is more energy efficient, sustainable, and robust. First, it avoids lack-of-fusion porosity from incomplete melting of powder particles, though it is crucial to note that this defect source is dominated by insufficient melt pool overlap (and is thus another example where energy density is inadequate as a metric) (Tang, Pistorius, and Beuth, 2017; Gordon *et al.*, 2020). Second, the laser beam undergoes multiple reflections inside the keyhole, which enhances laser absorption and improves energy efficiency (Trapp *et al.*, 2017; Simonds *et al.*, 2018; Allen *et al.*, 2020), particularly for highly reflective metals such as aluminum, copper, gold, and their alloys (Buchbinder *et al.*, 2011; Boley, Khairallah, and Rubenchik, 2015; Ikeshoji *et al.*, 2018; Jadhav *et al.*, 2021). Third, the keyhole attracts, captures, and removes nearby pores from various sources (like the powder and surfaces) because of thermocapillary force (Selva *et al.*, 2010; Brennen, 2013; Hojjatzadeh *et al.*, 2019; Leung *et al.*, 2019; Zhao *et al.*, 2020). Fourth, a stable keyhole tends to maintain its morphology and depth over time, having no distinct protrusions on the front keyhole wall, and changes in the laser and powder conditions will generally not disturb the stability (Cunningham *et al.*, 2019; Kouraytem *et al.*, 2019; Wang, Zhang, and Yan, 2020; Zhao *et al.*, 2020; Gan *et al.*, 2021). This expands the process window. Additionally, the mechanical and corrosion properties of the build could be strengthened as a result of the refinement of grain and phase structures (Roehling *et al.*, 2020; Lu *et al.*, 2021).

D. Process metrology

There is a significant need for improved process metrology in laser fusion AM of metals (Slotwinski and Garboczi, 2015; Mani *et al.*, 2017). The most relevant of these for accurate determination of melting modes are laser power, beam profile, and scan velocity (Hu and Mahadevan, 2017; Williams *et al.*, 2017). Together they determine the amount of energy delivered at any location during a build. For laser power, traditional thermal power meters with uncertainties typically in the range of 3%–5% are readily available (Williams *et al.*, 2021). However, such uncertainties are not often reported in the literature and the laser power is assumed to be what was requested by the user. The previously offered physics-based definitions point to the importance of laser irradiance in determining the melting modes. For an accurate determination of transferable process windows, we recommend that laser power be directly measured, and uncertainties stated, for every study that considers power as a variable.

The beam profile is also important for determining the melt pool outcomes, as simulations have shown (Yan *et al.*, 2020). In the literature, the generic term "spot size" is often simply stated. A single parameter like this can be used only if the geometric profile of the beam is known (to some uncertainty) and its definition explicitly stated (such as $1/e^2$ and $1/e$). Several commercial systems are currently available for measuring beam profiles, but there is no method of establishing absolute traceability, as there is with laser power, which presents a metrology opportunity whereby discrepancies between commercial beam profilers could be quantified and resolved.

Last, scan velocity plays an equally important role in determining the dwell time, and thus the energy delivered, during a laser scan. Nonetheless, little attention has been paid to its measurement or accuracy.

V. CONCLUSION

In this review, we have described the general physical process of laser melting. It is the complex interplay of many physical mechanisms caused by extreme thermal conditions that determines the vapor depression and melt pool morphologies and defines the melting mode. The melting mode changes with increasing temperature from conduction to transition to keyhole.

According to the morphology measurement approaches, the definitions of melting modes can be postmortem or process based. The postmortem-based definitions are conceptually reasonable but they are subjective, vague, and confusing because of the omission of the vapor depression details. By contrast, the process-based definitions, where the morphologies of both the melt pool and the vapor depression are measured directly from the *operando* high-speed x-ray images, are clearer and more complete. They solve the mystery of keyhole pores generated in the traditionally defined conduction mode.

The revision of the melting mode definitions suggests new guidelines and directions. First, in laser fusion AM of metals the laser-matter interactions are mainly with a vapor cavity. Beyond the conduction mode, the vapor depression is much more dynamic and transient than traditionally anticipated. Second, the stable-keyhole laser melting proposes an approach for sustainable and robust additive manufacturing. The boundaries and origins of some common defect generation zones in the *P*-*V* space are still lacking. In addition, multiphysics simulations, signal translations from morphology data to other feasible and complementary measurement signals, and improved process metrology are being used to develop transferable process windows across platforms and scales.

It is the *operando* high-speed x-ray imaging technique that opened the door to the physical process underlying the laser melting a few decades after the concept of keyholing was first proposed. With the technical advancement, it is possible to reexamine the long-standing problems at higher spatial, temporal, and energy resolutions and continue to update or revise the existing theories and models. We hope that this review will not only deepen the understanding of laser melting modes but also inspire the mind in frontier research and the development of laser fusion additive manufacturing of metals.

LIST OF SYMBOLS AND ABBREVIATIONS

AR	aspect ratio
AR_k	aspect ratio of vapor depression that defines the lower limit of keyhole mode in the updated version of the postmortem-based definitions
AR_m:	aspect ratio of melt pool that defines the lower limit of the keyhole mode in the original version of the postmortem-based definitions
AR_{sk}	aspect ratio of vapor depression that defines the lower limit of the transition mode in the process-based definitions
AR_{sm}	aspect ratio of melt pool that defines the lower limit of the keyhole mode in the process-based definitions
d	depth of a postmortem transverse cross section of the fused melt pool or a vapor depression
D	spot size of a laser beam
P	laser power
t	time
t_d	time point of the vapor depression or melt pool transition
T	peak temperature of melt pool
T_b	boiling point
T_c	a temperature below the boiling point that defines the lower limit of the keyhole mode in the original version of the postmortem-based definitions
T_m	melting point
T_s	peak temperature of melt pool at which the aspect ratio of the melt pool reaches AR_m in the updated version of the postmortem-based definitions
T_{sk}	peak temperature of the melt pool at which the aspect ratio of the vapor depression reaches AR_{sk} in the process-based definitions
T_{sm}	peak temperature of melt pool at which the aspect ratio of the melt pool reaches AR_{sm} in the process-based definitions
V	laser scan velocity
V_d	critical velocity point of the vapor depression or melt pool transition
w	width of a postmortem transverse cross section of the fused melt pool or a vapor depression
AM	additive manufacturing
APS	Advanced Photon Source
bcc	body-centered cubic
fcc	face-centered cubic
LPBF	laser powder bed fusion
Pro	protrusion structure on the front keyhole wall
Pro^+	protrusion structure tilting upward on the front keyhole wall
Pro^-	protrusion structure leaning downward on the front keyhole wall
RTS	reverse-triangle-like shape, describing a transient state of the keyhole bottom
SSRL	Stanford Synchrotron Radiation Lightsource
subs.	metal substrate

ACKNOWLEDGMENTS

We are grateful to I. Bitharas, F. D. Carlo, L. Chen, R. Cunningham, B. Gould, Q. Guo, N. Kouraytem, C. M. Kube, X. Li, N. Parab, W. Tan, and S. Wolff for stimulating collaborations. We thank N. Derimow and O. L. Kafka of the National Institute of Standards and Technology (NIST) for their careful review and feedback on this manuscript. We also thank B. Chang, A. Godfrey, F. Lin, and H. Xie at Tsinghua University for fruitful discussions. We are grateful to Y. Feng and Y. Huang and for assistance with the artwork in Figs. 6(b) and 7(b). C. Z., B. S., and S. C. acknowledge support from the National Natural Science Foundation of China (Grant No. 52175332), the Tsinghua-Imperial Research and Innovation Seed Fund, and the start-up fund of Tsinghua University. D. D. acknowledges support from the National Natural Science Foundation of China (Grant No. U1537205). T. S. acknowledges the start-up fund of the University of Virginia. A. D. R. acknowledges support from NASA's University Leadership Initiative (ULI) program under Grant No. 80NSSC19M0123. Synchrotron experiments in this contribution used resources of the Advanced Photon Source, a U.S. Department of Energy (DOE) Office of Science User Facility operated for the DOE Office of Science by Argonne National Laboratory under Contract No. DE-AC02-06CH11357.

APPENDIX: HIGH-SPEED SYNCHROTRON X-RAY IMAGING

The *operando* high-speed synchrotron x-ray imaging results of laser melting shown in Figs. 2 and 5 were obtained from a homebuilt experimental apparatus at the 32-ID-B beamline of the Advanced Photon Source (APS) at Argonne National Laboratory (Zhao *et al.*, 2017, 2022; Parab *et al.*, 2018). As shown in Fig. 8, it consists of an x-ray imaging system and a laser powder bed fusion simulator.

Generally, a short-period undulator (18 mm) with a gap of 12–14 mm is used to generate polychromatic x rays with the integrated flux of $\sim 7 \times 10^{15}$ photons/s and the first harmonic energy at ~24 keV (Fezzaa and Wang, 2008;

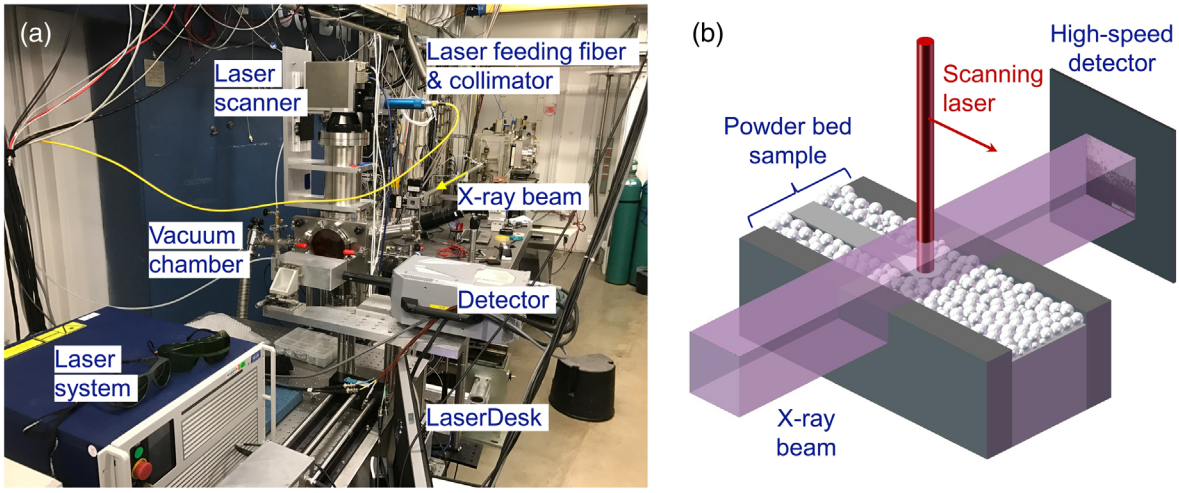

FIG. 8. Synchrotron x-ray imaging of laser melting. (a) Configuration of experimental systems. (b) Experimental schematic.

Wang *et al.*, 2008; Hudspeth *et al.*, 2015). The imaging system includes a 100 μm thick Lu3Al5O12:Ce scintillator, a 45° reflection mirror, a 10× objective lens (NA = 0.28, Edmund Optics, USA), a tube lens, and a Photron FastCam SA-Z camera (Fig. 5; Photron, Japan) or a Shimadzu HPV-X2 camera (Fig. 2; Shimadzu, Japan). The spatial resolution is 2 to 3 μm/pixel, the minimum effective exposure time for each x-ray image is a single x-ray pulse (∼100 ps), and the maximum effective frame rate is 6.5×10^6 frames/s.

In a typical laser melting experiment, a powder bed sample, which is made of two identical pieces of glassy carbon (vitreous) plates, one metal base, and one layer of metal powder, is loaded into a custom-built vacuum chamber, with the sample thickness along the x-ray direction and the thickness centerline on the laser scanning plane (Zhao *et al.*, 2017). The sample thickness needs to be optimized to properly image the real fusion process. In practice, a series of samples having various thicknesses from hundreds of microns to a few millimeters should be used to confirm that the keyhole morphology and depth under given laser conditions have no detectable difference between the chosen sample and the bulkier sample. The chamber is then pumped down and purged with pure argon gas back to atmospheric pressure. The laser heating system consists of an ytterbium fiber laser (IPG YLR-500-AC, USA) and a galvo laser scanner (intelliSCANde 30, SCANLAB GmbH, Germany).[1] The fiber laser is in a single mode providing pure Gaussian beam profiles. The wavelength and the maximum laser power are 1070 nm and 560 W, respectively. With a $f/340$ mm objective lens and a $f/85$ mm collimator, the laser-beam spot size is 50 ± 5 μm ($1/e^2$) at the focal plane. The actual spot size on the sample surface is controlled by defocusing. The scan speed of the scanner at the focal plane could reach 2.0 m/s.

During the experiment, the laser is often operated in continuous-wave mode and scans along a single straight line to heat the metal sample. Simultaneously, the x-ray beam penetrates through the sample and provides a side view of the laser melting through both absorption and phase contrasts (Wilkins *et al.*, 1996; Fezzaa and Wang, 2008; Wang *et al.*, 2008), from which the melt pool and vapor depression morphologies can be identified and measured.

In addition to the APS, intensive research activities at other synchrotron facilities have been conducted around the world in recent years to study the metal additive manufacturing process. These facilities include the Diamond Light Source, the Stanford Synchrotron Radiation Lightsource, the European Synchrotron Radiation Facility, Super Photon ring-8 GeV, and the Swiss Light Source (Calta *et al.*, 2018; Leung *et al.*, 2018; Miyagi *et al.*, 2018; Martin *et al.*, 2019a; Hocine *et al.*, 2020). They have largely promoted a fundamental understanding of various physical phenomena, microstructures, and defects in laser fusion of metals.

[1]Certain commercial equipment, instruments, and/or materials are identified in this review to specify the experimental procedure. Such identification does not imply recommendation or endorsement by the National Institute of Standards and Technology.

REFERENCES

Aboulkhair, N. T., N. M. Everitt, I. Ashcroft, and C. Tuck, 2014, "Reducing porosity in AlSi10Mg parts processed by selective laser melting," Addit. Manuf. **1–4**, 77–86.

Aboulkhair, N. T., I. Maskery, C. Tuck, I. Ashcroft, and N. M. Everitt, 2016, "On the formation of AlSi10Mg single tracks and layers in selective laser melting: Microstructure and nano-mechanical properties," J. Mater. Process. Technol. **230**, 88–98.

Agrawal, P., S. Thapliyal, S. S. Nene, R. S. Mishra, B. A. McWilliams, and K. C. Cho, 2020, "Excellent strength-ductility synergy in metastable high entropy alloy by laser powder bed additive manufacturing," Addit. Manuf. **32**, 101098.

Allen, T. R., W. Huang, J. R. Tanner, W. Tan, J. M. Fraser, and B. J. Simonds, 2020, "Energy-Coupling Mechanisms Revealed through Simultaneous Keyhole Depth and Absorptance Measurements during Laser-Metal Processing," Phys. Rev. Applied **13**, 064070.

Amara, E. H., and R. Fabbro, 2010, "Modeling of humps formation during deep-penetration laser welding," Appl. Phys. A **101**, 111–116.

Anisimov, S. I., and V. A. Khokhlov, 1995, *Instabilities in Laser-Matter Interaction* (CRC Press, Boca Raton).

Assuncao, E., S. Williams, and D. Yapp, 2012, "Interaction time and beam diameter effects on the conduction mode limit," Opt. Lasers Eng. **50**, 823–828.

ASTM International, 2021, Report No. ISO/ASTM 52900:2021.

Atwood, C., M. Griffith, L. Harwell, E. Schlienger, M. Ensz, J. Smugeresky, T. Romero, D. Greene, and D. Reckaway, 1998, "Laser engineered net shaping (LENS™): A tool for direct fabrication of metal parts," in *Proceedings of the Laser Materials Processing Conference (ICALEO '98), Orlando, 1998*, edited by E. Beyer, X. Chen, and I. Miyamoto, pp. E1–E7, 10.2351/1.5059147.

Bauereiß, A., T. Scharowsky, and C. Körner, 2014, "Defect generation and propagation mechanism during additive manufacturing by selective beam melting," J. Mater. Process. Technol. **214**, 2522–2528.

Bayat, M., A. Thanki, S. Mohanty, A. Witvrouw, S. Yang, J. Thorborg, N. S. Tiedje, and J. H. Hattel, 2019, "Keyhole-induced porosities in laser-based powder bed fusion (L-PBF) of Ti6Al4V: High-fidelity modelling and experimental validation," Addit. Manuf. **30**, 100835.

Beuth, J., *et al.*, 2013, "Process mapping for qualification across multiple direct metal additive manufacturing processes," in *Proceedings of the 24th International Solid Freeform Fabrication Symposium, Austin, 2013*, edited by D. L. Bourell (University of Texas Press, Austin), pp. 655–665, 10.26153/tsw/15590.

Bidare, P., I. Bitharas, R. M. Ward, M. M. Attallah, and A. J. Moore, 2018, "Fluid and particle dynamics in laser powder bed fusion," Acta Mater. **142**, 107–120.

Bitharas, I., N. Parab, C. Zhao, T. Sun, A. D. Rollett, and A. J. Moore, 2022, "The interplay between vapour, liquid, and solid phases in laser powder bed fusion," Nat. Commun. **13**, 2959.

Boettinger, W. J., D. Shechtman, R. J. Schaefer, and F. S. Biancaniello, 1984, "The effect of rapid solidification velocity on the microstructure of Ag-Cu alloys," Metall. Trans. A **15**, 55–66.

Boley, C. D., S. A. Khairallah, and A. M. Rubenchik, 2015, "Calculation of laser absorption by metal powders in additive manufacturing," Appl. Opt. **54**, 2477–2482.

Bontha, S., N. W. Klingbeil, P. A. Kobryn, and H. L. Fraser, 2006, "Thermal process maps for predicting solidification microstructure in laser fabrication of thin-wall structures," J. Mater. Process. Technol. **178**, 135–142.

Brennen, C. E., 2013, *Cavitation and Bubble Dynamics* (Cambridge University Press, Cambridge, England).

Brika, S. E., M. Letenneur, C. A. Dion, and V. Brailovski, 2020, "Influence of particle morphology and size distribution on the powder flowability and laser powder bed fusion manufacturability of Ti-6Al-4V alloy," Addit. Manuf. **31**, 100929.

Brown, M. S., and C. B. Arnold, 2010, "Fundamentals of laser-material interaction and application to multiscale surface modification," in *Laser Precision Microfabrication*, edited by K. Sugioka, M. Meunier, and A. Piqué (Springer, Berlin), pp. 91–120.

Buchbinder, D., H. Schleifenbaum, S. Heidrich, W. Meiners, and J. Bültmann, 2011, "High power selective laser melting (HP SLM) of aluminum parts," Phys. Procedia **12**, 271–278.

Calta, N. P., *et al.*, 2018, "An instrument for *in situ* time-resolved x-ray imaging and diffraction of laser powder bed fusion additive manufacturing processes," Rev. Sci. Instrum. **89**, 055101.

Campbell, F. C., 2008, Ed., *Elements of Metallurgy and Engineering Alloys* (ASM International, Materials Park, OH), 10.31399/asm.tb.emea.9781627082518.

Campbell, I., D. Bourell, and I. Gibson, 2012, "Additive manufacturing: Rapid prototyping comes of age," Rapid Prototyp. J. **18**, 255–258.

Chandrasekhar, S., 1981, *Hydrodynamic and Hydromagnetic Stability* (Dover Publications, New York).

Chen, Y., S. J. Clark, C. L. A. Leung, L. Sinclair, S. Marussi, M. P. Olbinado, E. Boller, A. Rack, I. Todd, and P. D. Lee, 2020, "*In-situ* synchrotron imaging of keyhole mode multi-layer laser powder bed fusion additive manufacturing," Appl. Mater. Today **20**, 100650.

Chiang, P. J., R. Jiang, R. Cunningham, N. Parab, C. Zhao, K. Fezzaa, T. Sun, and A. D. Rollett, 2019, "*In situ* characterization of hot cracking using dynamic x-ray radiography," in *Advanced Real Time Imaging II*, edited by J. Nakano, P. C. Pistorius, C. Tamerler, H. Yasuda, Z. Zhang, N. Dogan, W. Wang, N. Saito, and B. Webler (Springer International Publishing, Cham, Switzerland), pp. 77–85, https://link.springer.com/chapter/10.1007/978-3-030-06143-2_8.

Cho, J. H., and S. J. Na, 2006, "Implementation of real-time multiple reflection and Fresnel absorption of laser beam in keyhole," J. Phys. D **39**, 5372–5378.

Cook, P. S., and A. B. Murphy, 2020, "Simulation of melt pool behaviour during additive manufacturing: Underlying physics and progress," Addit. Manuf. **31**, 100909.

Cunningham, R., S. P. Narra, C. Montgomery, J. Beuth, and A. D. Rollett, 2017, "Synchrotron-based x-ray microtomography characterization of the effect of processing variables on porosity formation in laser powder-bed additive manufacturing of Ti-6Al-4V," JOM **69**, 479–484.

Cunningham, R., S. P. Narra, T. Ozturk, J. Beuth, and A. D. Rollett, 2016, "Evaluating the effect of processing parameters on porosity in electron beam melted Ti-6Al-4V via synchrotron x-ray microtomography," JOM **68**, 765–771.

Cunningham, R., A. Nicolas, J. Madsen, E. Fodran, E. Anagnostou, M. D. Sangid, and A. D. Rollett, 2017, "Analyzing the effects of powder and post-processing on porosity and properties of electron beam melted Ti-6Al-4V," Mater. Res. Lett. **5**, 516–525.

Cunningham, R., C. Zhao, N. Parab, C. Kantzos, J. Pauza, K. Fezzaa, T. Sun, and A. D. Rollett, 2019, "Keyhole threshold and morphology in laser melting revealed by ultrahigh-speed x-ray imaging," Science **363**, 849–852.

Daeneke, T., K. Khoshmanesh, N. Mahmood, I. A. de Castro, D. Esrafilzadeh, S. J. Barrow, M. D. Dickey, and K. Kalantar-zadeh, 2018, "Liquid metals: Fundamentals and applications in chemistry," Chem. Soc. Rev. **47**, 4073–4111.

DebRoy, T., T. Mukherjee, H. L. Wei, J. W. Elmer, and J. O. Milewski, 2021, "Metallurgy, mechanistic models and machine learning in metal printing," Nat. Rev. Mater. **6**, 48–68.

DebRoy, T., H. L. Wei, J. S. Zuback, T. Mukherjee, J. W. Elmer, J. O. Milewski, A. M. Beese, A. Wilson-Heid, A. De, and W. Zhang, 2018, "Additive manufacturing of metallic components—Process, structure and properties," Prog. Mater. Sci. **92**, 112–224.

Derimow, N., E. J. Schwalbach, J. T. Benzing, J. P. Killgore, A. B. Artusio-Glimpse, N. Hrabe, and B. J. Simonds, 2022, "*In situ* absorption synchrotron measurements, predictive modeling, microstructural analysis, and scanning probe measurements of laser melted Ti-6Al-4V single tracks for additive manufacturing applications," J. Alloys Compd. **900**, 163494.

Doubenskaia, M., M. Pavlov, S. Grigoriev, and I. Smurov, 2013, "Definition of brightness temperature and restoration of true temperature in laser cladding using infrared camera," Surf. Coat. Technol. **220**, 244–247.

Dowden, J, 2017, "Laser keyhole welding: The vapour phase," in *The Theory of Laser Materials Processing: Heat and Mass Transfer in Modern Technology*, edited by J. Dowden and W. Schulz (Springer International Publishing, Cham, Switzerland), pp. 95–128.

Dowden, J., M. Davis, and P. Kapadia, 1985, "The flow of heat and the motion of the weld pool in penetration welding with a laser," J. Appl. Phys. **57**, 4474–4479.

Dowling, L., J. Kennedy, S. O'Shaughnessy, and D. Trimble, 2020, "A review of critical repeatability and reproducibility issues in powder bed fusion," Mater. Des. **186**, 108346.

Eagar, T., and N. Tsai, 1983, "Temperature fields produced by traveling distributed heat sources," Weld. J. **62**, 346–355, https://app.aws.org/wj/supplement/WJ_1983_12_s346.pdf.

Elmer, J. W., P. W. Hochanadel, K. Lachenberg, C. Caristan, and T. Webber, 2011, "Introduction to high energy density electron and laser beam welding," in *Welding Fundamentals and Processes*, edited by T. Lienert, T. Siewert, S. Babu, and V. Acoff (ASM International, Materials Park, OH), pp. 507–513, 10.31399/asm.hb.v06a.a0005627.

El-Sayed, M. A., 2001, "Some interesting properties of metals confined in time and nanometer space of different shapes," Acc. Chem. Res. **34**, 257–264.

Fabbro, R., and K. Chouf, 2000, "Keyhole modeling during laser welding," J. Appl. Phys. **87**, 4075–4083.

Fabbro, R., M. Dal, P. Peyre, F. Coste, M. Schneider, and V. Gunenthiram, 2018, "Analysis and possible estimation of keyhole depths evolution, using laser operating parameters and material properties," J. Laser Appl. **30**, 032410.

Fabbro, R., S. Slimani, I. Doudet, F. Coste, and F. Briand, 2006, "Experimental study of the dynamical coupling between the induced vapour plume and the melt pool for Nd–Yag CW laser welding," J. Phys. D **39**, 394–400.

Farshidianfar, M. H., A. Khajepour, and A. P. Gerlich, 2016, "Effect of real-time cooling rate on microstructure in laser additive manufacturing," J. Mater. Process. Technol. **231**, 468–478.

Fezzaa, K., and Y. Wang, 2008, "Ultrafast X-Ray Phase-Contrast Imaging of the Initial Coalescence Phase of Two Water Droplets," Phys. Rev. Lett. **100**, 104501.

Forien, J. B., N. P. Calta, P. J. DePond, G. M. Guss, T. T. Roehling, and M. J. Matthews, 2020, "Detecting keyhole pore defects and monitoring process signatures during laser powder bed fusion: A correlation between *in situ* pyrometry and *ex situ* x-ray radiography," Addit. Manuf. **35**, 101336.

Foroozmehr, A., M. Badrossamay, E. Foroozmehr, and S. Golabi, 2016, "Finite element simulation of selective laser melting process considering optical penetration depth of laser in powder bed," Mater. Des. **89**, 255–263.

Frazier, W. E., 2014, "Metal additive manufacturing: A review," J. Mater. Eng. Perform. **23**, 1917–1928.

Gan, Z., O. L. Kafka, N. Parab, C. Zhao, L. Fang, O. Heinonen, T. Sun, and W. K. Liu, 2021, "Universal scaling laws of keyhole stability and porosity in 3D printing of metals," Nat. Commun. **12**, 2379.

Gäumann, M., S. Henry, F. Cléton, J. D. Wagnière, and W. Kurz, 1999, "Epitaxial laser metal forming: Analysis of microstructure formation," Mater. Sci. Eng. A **271**, 232–241.

Gaynor, A. T., and J. K. Guest, 2016, "Topology optimization considering overhang constraints: Eliminating sacrificial support material in additive manufacturing through design," Struct. Multidiscipl. Optim. **54**, 1157–1172.

Gillespie, J., W. Y. Yeoh, C. Zhao, N. D. Parab, T. Sun, A. D. Rollett, B. Lan, and C. M. Kube, 2021, "*In situ* characterization of laser-generated melt pools using synchronized ultrasound and high-speed x-ray imaging," J. Acoust. Soc. Am. **150**, 2409–2420.

Gisario, A., M. Kazarian, F. Martina, and M. Mehrpouya, 2019, "Metal additive manufacturing in the commercial aviation industry: A review," J. Manuf. Syst. **53**, 124–149.

Gong, H., K. Rafi, H. Gu, T. Starr, and B. Stucker, 2014, "Analysis of defect generation in Ti–6Al–4V parts made using powder bed fusion additive manufacturing processes," Addit. Manuf. **1–4**, 87–98.

Gordon, J. V., S. P. Narra, R. W. Cunningham, H. Liu, H. Chen, R. M. Suter, J. L. Beuth, and A. D. Rollett, 2020, "Defect structure process maps for laser powder bed fusion additive manufacturing," Addit. Manuf. **36**, 101552.

Griffith, M. L., D. M. Keicher, C. L. Atwood, J. A. Romero, J. E. Smugeresky, L. D. Harwell, and D. L. Greene, 1996, "Free form fabrication of metallic components using laser engineered net shaping (LENS™)," in *Proceedings of the Seventh Solid Freeform Fabrication Symposium, Austin, 1996*, edited by D. Bourell, J. Beaman, H. Marcus, R. Crawford, and J. Barlow (University of Texas Press, Austin), pp. 125–132, https://repositories.lib.utexas.edu/handle/2152/69929.

Griffith, M. L., *et al.*, 1999, "Understanding thermal behavior in the LENS process," Mater. Des. **20**, 107–113.

Gu, D., and Y. Shen, 2007, "Balling phenomena during direct laser sintering of multi-component Cu-based metal powder," J. Alloys Compd. **432**, 163–166.

Gu, D., X. Shi, R. Poprawe, D. L. Bourell, R. Setchi, and J. Zhu, 2021, "Material-structure-performance integrated laser-metal additive manufacturing," Science **372**, eabg1487.

Guo, Q., C. Zhao, L. I. Escano, Z. Young, L. Xiong, K. Fezzaa, W. Everhart, B. Brown, T. Sun, and L. Chen, 2018, "Transient dynamics of powder spattering in laser powder bed fusion additive manufacturing process revealed by *in-situ* high-speed high-energy x-ray imaging," Acta Mater. **151**, 169–180.

Gür, C. H., and J. Pan, 2008, Eds., *Handbook of Thermal Process Modeling Steels* (CRC Press, Boca Raton), https://www.taylorfrancis.com/books/mono/10.1201/9781420003581/handbook-thermal-process-modeling-steels-cemil-hakan-gur-jiansheng-pan.

Gusarov, A. V., and I. Smurov, 2010, "Modeling the interaction of laser radiation with powder bed at selective laser melting," Phys. Procedia **5**, 381–394.

Heiden, M. J., L. A. Deibler, J. M. Rodelas, J. R. Koepke, D. J. Tung, D. J. Saiz, and B. H. Jared, 2019, "Evolution of 316L stainless steel feedstock due to laser powder bed fusion process," Addit. Manuf. **25**, 84–103.

Heigel, J. C., B. M. Lane, and L. E. Levine, 2020, "*In situ* measurements of melt-pool length and cooling rate during 3D builds of the metal AM-bench artifacts," Integr. Mater. Manuf. Innov. **9**, 31–53.

Herzog, D., V. Seyda, E. Wycisk, and C. Emmelmann, 2016, "Additive manufacturing of metals," Acta Mater. **117**, 371–392.

Hirano, K., R. Fabbro, and M. Muller, 2011, "Experimental determination of temperature threshold for melt surface deformation during laser interaction on iron at atmospheric pressure," J. Phys. D **44**, 435402.

Hocine, S., H. Van Swygenhoven, S. Van Petegem, C. S. T. Chang, T. Maimaitiyili, G. Tinti, D. F. Sanchez, D. Grolimund, and N. Casati, 2020, "*Operando* x-ray diffraction during laser 3D printing," Mater. Today **34**, 30–40.

Hojjatzadeh, S. M. H., *et al.*, 2019, "Pore elimination mechanisms during 3D printing of metals," Nat. Commun. **10**, 3088.

Hojjatzadeh, S. M. H., *et al.*, 2020, "Direct observation of pore formation mechanisms during LPBF additive manufacturing process and high energy density laser welding," Int. J. Mach. Tools Manuf. **153**, 103555.

Hooper, P. A., 2018, "Melt pool temperature and cooling rates in laser powder bed fusion," Addit. Manuf. **22**, 548–559.

Hossain, M. S., J. A. Gonzalez, R. M. Hernandez, M. A. I. Shuvo, J. Mireles, A. Choudhuri, Y. Lin, and R. B. Wicker, 2016, "Fabrication of smart parts using powder bed fusion additive manufacturing technology," Addit. Manuf. **10**, 58–66.

Hou, J., B. Dai, Y. Li, J. Zhao, Z. Chen, D. Pan, Y. Zhu, K. Zhang, and A. Huang, 2020, "Helium bubble nucleation in laser powder bed fusion processed 304L stainless steel," J. Nucl. Mater. **542**, 152443.

Hu, Y. N., S. C. Wu, P. J. Withers, J. Zhang, H. Y. X. Bao, Y. N. Fu, and G. Z. Kang, 2020, "The effect of manufacturing defects on the fatigue life of selective laser melted Ti-6Al-4V structures," Mater. Des. **192**, 108708.

Hu, Z., and S. Mahadevan, 2017, "Uncertainty quantification and management in additive manufacturing: Current status, needs, and opportunities," Int. J. Adv. Manuf. Technol. **93**, 2855–2874.

Huang, Y., T. G. Fleming, S. J. Clark, S. Marussi, K. Fezzaa, J. Thiyagalingam, C. L. A. Leung, and P. D. Lee, 2022, "Keyhole fluctuation and pore formation mechanisms during laser powder bed fusion additive manufacturing," Nat. Commun. **13**, 1170.

Hudspeth, M., T. Sun, N. Parab, Z. Guo, K. Fezzaa, S. Luo, and W. Chen, 2015, "Simultaneous x-ray diffraction and phase-contrast imaging for investigating material deformation mechanisms during high-rate loading," J. Synchrotron Radiat. **22**, 49–58.

Iebba, M., A. Astarita, D. Mistretta, I. Colonna, M. Liberini, F. Scherillo, C. Pirozzi, R. Borrelli, S. Franchitti, and A. Squillace, 2017, "Influence of powder characteristics on formation of porosity in additive manufacturing of Ti-6Al-4V components," J. Mater. Eng. Perform. **26**, 4138–4147.

Ikeshoji, T. T., K. Nakamura, M. Yonehara, K. Imai, and H. Kyogoku, 2018, "Selective laser melting of pure copper," JOM **70**, 396–400.

Ion, J. C., H. R. Shercliff, and M. F. Ashby, 1992, "Diagrams for laser materials processing," Acta Metall. Mater. **40**, 1539–1551.

Islam, M., T. Purtonen, H. Piili, A. Salminen, and O. Nyrhilä, 2013, "Temperature profile and imaging analysis of laser additive manufacturing of stainless steel," Phys. Procedia **41**, 835–842.

Jadhav, S. D., L. R. Goossens, Y. Kinds, B. V. Hooreweder, and K. Vanmeensel, 2021, "Laser-based powder bed fusion additive manufacturing of pure copper," Addit. Manuf. **42**, 101990.

Joint Defense Manufacturing Council, 2021, "Department of Defense additive manufacturing strategy," report, https://www.cto.mil/wp-content/uploads/2021/01/dod-additive-manufacturing-strategy.pdf.

Juhasz, M., R. Tiedemann, G. Dumstorff, J. Walker, A. D. Plessis, B. Conner, W. Lang, and E. MacDonald, 2020, "Hybrid directed energy deposition for fabricating metal structures with embedded sensors," Addit. Manuf. **35**, 101397.

Kaplan, A., 1994, "A model of deep penetration laser welding based on calculation of the keyhole profile," J. Phys. D **27**, 1805.

Kenel, C., D. Grolimund, X. Li, E. Panepucci, V. A. Samson, D. F. Sanchez, F. Marone, and C. Leinenbach, 2017, "*In situ* investigation of phase transformations in Ti-6Al-4V under additive manufacturing conditions combining laser melting and high-speed micro-x-ray diffraction," Sci. Rep. **7**, 16358.

Khairallah, S. A., A. T. Anderson, A. Rubenchik, and W. E. King, 2016, "Laser powder-bed fusion additive manufacturing: Physics of complex melt flow and formation mechanisms of pores, spatter, and denudation zones," Acta Mater. **108**, 36–45.

Khairallah, S. A., T. Sun, and B. J. Simonds, 2021, "Onset of periodic oscillations as a precursor of a transition to pore-generating turbulence in laser melting," Addit. Manuf. Lett. **1**, 100002.

Khairallah, S. A., *et al.*, 2020, "Controlling interdependent meso-nanosecond dynamics and defect generation in metal 3D printing," Science **368**, 660.

Ki, H., J. Mazumder, and P. S. Mohanty, 2002, "Modeling of laser keyhole welding: Part I. mathematical modeling, numerical methodology, role of recoil pressure, multiple reflections, and free surface evolution," Metall. Mater. Trans. A **33**, 1817–1830.

King, W. E., A. T. Anderson, R. M. Ferencz, N. E. Hodge, C. Kamath, S. A. Khairallah, and A. M. Rubenchik, 2015, "Laser powder bed fusion additive manufacturing of metals; physics, computational, and materials challenges," Appl. Phys. Rev. **2**, 041304.

King, W. E., H. D. Barth, V. M. Castillo, G. F. Gallegos, J. W. Gibbs, D. E. Hahn, C. Kamath, and A. M. Rubenchik, 2014, "Observation of keyhole-mode laser melting in laser powder-bed fusion additive manufacturing," J. Mater. Process. Technol. **214**, 2915–2925.

Kiss, A. M., *et al.*, 2019, "Laser-induced keyhole defect dynamics during metal additive manufacturing," Adv. Eng. Mater. **21**, 1900455.

Kosonen, T., K. Kakko, and N. Raitanen, 2021, "Evaluation of pore re-opening after HIP in LPBF Ti–6Al–4V," Powder Metall. **64**, 425–433.

Kouraytem, N., X. Li, R. Cunningham, C. Zhao, N. Parab, T. Sun, A. D. Rollett, A. D. Spear, and W. Tan, 2019, "Effect of Laser-Matter Interaction on Molten Pool Flow and Keyhole Dynamics," Phys. Rev. Applied **11**, 064054.

Kroos, J., U. Gratzke, and G. Simon, 1993, "Towards a self-consistent model of the keyhole in penetration laser beam welding," J. Phys. D **26**, 474.

Kruth, J. P., L. Froyen, J. Van Vaerenbergh, P. Mercelis, M. Rombouts, and B. Lauwers, 2004, "Selective laser melting of iron-based powder," J. Mater. Process. Technol. **149**, 616–622.

Kruth, J. P., M. C. Leu, and T. Nakagawa, 1998, "Progress in additive manufacturing and rapid prototyping," CIRP Ann. **47**, 525–540.

Kruth, J. P., P. Mercelis, J. Van Vaerenbergh, L. Froyen, and M. Rombouts, 2005, "Binding mechanisms in selective laser sintering and selective laser melting," Rapid Prototyp. J. **11**, 26–36.

Kurpjuweit, S., C. G. Schmidt, M. Klöckner, and S. M. Wagner, 2021, "Blockchain in additive manufacturing and its impact on supply chains," J. Bus. Logist. **42**, 46–70.

Kurz, W., B. Giovanola, and R. Trivedi, 1986, "Theory of microstructural development during rapid solidification," Acta Metall. **34**, 823–830.

Kyo, M., E. Hiyazaki, S. Tsukioka, H. Ochi, Y. Amitani, T. Tsuchiya, T. Aoki, and S. Takagawa, 1995, "The sea trial of 'KAIKO,' the full ocean depth research ROV," in *Proceedings of OCEANS '95 MTS/IEEE, San Diego, 1995* (IEEE, New York), pp. 1991–1996, https://ieeexplore.ieee.org/abstract/document/528882/citations#citations.

Laleh, M., A. E. Hughes, S. Yang, J. Wang, J. Li, A. M. Glenn, W. Xu, and M. Y. Tan, 2021, "A critical insight into lack-of-fusion pore structures in additively manufactured stainless steel," Addit. Manuf. **38**, 101762.

Leach, R. K., D. Bourell, S. Carmignato, A. Donmez, N. Senin, and W. Dewulf, 2019, "Geometrical metrology for metal additive manufacturing," CIRP Ann. **68**, 677–700.

Lee, J. Y., S. H. Ko, D. F. Farson, and C. D. Yoo, 2002, "Mechanism of keyhole formation and stability in stationary laser welding," J. Phys. D **35**, 1570–1576.

Leung, C. L. A., S. Marussi, R. C. Atwood, M. Towrie, P. J. Withers, and P. D. Lee, 2018, "*In situ* x-ray imaging of defect and molten pool dynamics in laser additive manufacturing," Nat. Commun. **9**, 1355.

Leung, C. L. A., S. Marussi, M. Towrie, R. C. Atwood, P. J. Withers, and P. D. Lee, 2019, "The effect of powder oxidation on defect

formation in laser additive manufacturing," Acta Mater. **166**, 294–305.

Lewis, G. K., R. Nemec, J. Milewski, D. J. Thoma, D. Cremers, and M. Barbe, 1994, "Directed light fabrication," in *Proceedings of the Laser Materials Processing Conference (ICALEO '94), Orlando, 1994*, edited by T. Dwayne McCay, A. Matsunawa, and H. Hügel, pp. 17–26, 10.2351/1.5058786.

Lewis, G. K., and E. Schlienger, 2000, "Practical considerations and capabilities for laser assisted direct metal deposition," Mater. Des. **21**, 417–423.

Li, X., C. Zhao, T. Sun, and W. Tan, 2020, "Revealing transient powder-gas interaction in laser powder bed fusion process through multi-physics modeling and high-speed synchrotron x-ray imaging," Addit. Manuf. **35**, 101362.

Lide, D. R., 2004, Ed., *CRC Handbook of Chemistry and Physics*, 85th ed. (CRC Press, Boca Raton).

Lin, S., Z. Gan, J. Yan, and G. J. Wagner, 2020, "A conservative level set method on unstructured meshes for modeling multiphase thermo-fluid flow in additive manufacturing processes," Comput. Methods Appl. Mech. Eng. **372**, 113348.

Link, S., C. Burda, M. B. Mohamed, B. Nikoobakht, and M. A. El-Sayed, 1999, "Laser photothermal melting and fragmentation of gold nanorods: Energy and laser pulse-width dependence," J. Phys. Chem. A **103**, 1165–1170.

Liu, D. R., S. Wang, and W. Yan, 2020, "Grain structure evolution in transition-mode melting in direct energy deposition," Mater. Des. **194**, 108919.

Liu, S., and Y. C. Shin, 2019, "Additive manufacturing of Ti6Al4V alloy: A review," Mater. Des. **164**, 107552.

Lorazo, P., L. J. Lewis, and M. Meunier, 2003, "Short-Pulse Laser Ablation of Solids: From Phase Explosion to Fragmentation," Phys. Rev. Lett. **91**, 225502.

Lu, J., X. Lin, N. Kang, Y. Cao, Q. Wang, and W. Huang, 2021, "Keyhole mode induced simultaneous improvement in strength and ductility of Sc modified Al–Mn alloy manufactured by selective laser melting," Mater. Sci. Eng. A **811**, 141089.

Ly, S., A. M. Rubenchik, S. A. Khairallah, G. Guss, and M. J. Matthews, 2017, "Metal vapor micro-jet controls material redistribution in laser powder bed fusion additive manufacturing," Sci. Rep. **7**, 4085.

MacDonald, E., and R. Wicker, 2016, "Multiprocess 3D printing for increasing component functionality," Science **353**, aaf2093.

Maconachie, T., M. Leary, B. Lozanovski, X. Zhang, M. Qian, O. Faruque, and M. Brandt, 2019, "SLM lattice structures: Properties, performance, applications and challenges," Mater. Des. **183**, 108137.

Mani, M., B. M. Lane, M. A. Donmez, S. C. Feng, and S. P. Moylan, 2017, "A review on measurement science needs for real-time control of additive manufacturing metal powder bed fusion processes," Int. J. Prod. Res. **55**, 1400–1418.

Markl, M., and C. Körner, 2016, "Multiscale modeling of powder bed–based additive manufacturing," Annu. Rev. Mater. Res. **46**, 93–123.

Martin, A. A., *et al.*, 2019a, "Dynamics of pore formation during laser powder bed fusion additive manufacturing," Nat. Commun. **10**, 1987.

Martin, A. A., *et al.*, 2019b, "Ultrafast dynamics of laser-metal interactions in additive manufacturing alloys captured by *in situ* x-ray imaging," Mater. Today Adv. **1**, 100002.

Martin, A. A., *et al.*, 2021, "Enhanced mechanical performance via laser induced nanostructure formation in an additively manufactured lightweight aluminum alloy," Appl. Mater. Today **22**, 100972.

Martin, J. H., B. D. Yahata, J. M. Hundley, J. A. Mayer, T. A. Schaedler, and T. M. Pollock, 2017, "3D printing of high-strength aluminium alloys," Nature (London) **549**, 365–369.

Matsunawa, A., J. D. Kim, N. Seto, M. Mizutani, and S. Katayama, 1998, "Dynamics of keyhole and molten pool in laser welding," J. Laser Appl. **10**, 247–254.

McEnerney, B., R. P. Dillon, J. Vickers, K. M. Taminger, S. D. Jolly, and A. Rollett, 2021, "Enabling new science mission capabilities with additive manufacturing technologies," Bull. Am. Astron. Soc. **53**, 466.

Miller, K. J., and T. Takenaka, 1964, *Electron Beam Welding* (Welding Research Council Bulletin, New York).

Miotello, A., and R. Kelly, 1999, "Laser-induced phase explosion: New physical problems when a condensed phase approaches the thermodynamic critical temperature," Appl. Phys. A **69**, S67–S73.

Miyagi, M., Y. Kawahito, H. Wang, H. Kawakami, T. Shoubu, and M. Tsukamoto, 2018, "X-ray phase contrast observation of solidification and hot crack propagation in laser spot welding of aluminum alloy," Opt. Express **26**, 22626–22636.

Mohr, M., R. Wunderlich, R. Novakovic, E. Ricci, and H.-J. Fecht, 2020, "Precise measurements of thermophysical properties of liquid Ti–6Al–4V (Ti64) alloy on board the International Space Station," Adv. Eng. Mater. **22**, 2000169.

Mostafaei, A., *et al.*, 2022, "Defects and anomalies in powder bed fusion metal additive manufacturing," Curr. Opin. Solid State Mater. Sci. **26**, 100974.

Norris, J. T., and C. V. Robino, 2008, "Development of a time resolved energy absorption measurement technique for laser beam spot welds," in *Proceedings of the 27th International Congress on Laser Materials Processing, Laser Microprocessing and Nanomanufacturing (ICALEO '08), Temecula, CA, 2008*, p. 149, 10.2351/1.5061443.

Onuike, B., B. Heer, and A. Bandyopadhyay, 2018, "Additive manufacturing of Inconel 718—Copper alloy bimetallic structure using laser engineered net shaping (LENS™)," Addit. Manuf. **21**, 133–140.

Panwisawas, C., B. Perumal, R. M. Ward, N. Turner, R. P. Turner, J. W. Brooks, and H. C. Basoalto, 2017, "Keyhole formation and thermal fluid flow-induced porosity during laser fusion welding in titanium alloys: Experimental and modelling," Acta Mater. **126**, 251–263.

Panwisawas, C., Y. T. Tang, and R. C. Reed, 2020, "Metal 3D printing as a disruptive technology for superalloys," Nat. Commun. **11**, 2327.

Parab, N. D., C. Zhao, R. Cunningham, L. I. Escano, K. Fezzaa, W. Everhart, A. D. Rollett, L. Chen, and T. Sun, 2018, "Ultrafast x-ray imaging of laser–metal additive manufacturing processes," J. Synchrotron Radiat. **25**, 1467–1477.

Patel, S., and M. Vlasea, 2020, "Melting modes in laser powder bed fusion," Materialia **9**, 100591.

Paul, A., and T. Debroy, 1988, "Free surface flow and heat transfer in conduction mode laser welding," Metall. Trans. B **19**, 851–858.

Pollock, T. M., A. J. Clarke, and S. S. Babu, 2020, "Design and tailoring of alloys for additive manufacturing," Metall. Mater. Trans. A **51**, 6000–6019.

Polonsky, A. T., W. C. Lenthe, M. P. Echlin, V. Livescu, G. T. Gray, and T. M. Pollock, 2020, "Solidification-driven orientation gradients in additively manufactured stainless steel," Acta Mater. **183**, 249–260.

Polonsky, A. T., and T. M. Pollock, 2020, "Closing the science gap in 3D metal printing," Science **368**, 583–584.

Pordzik, R., and P. Woizeschke, 2020, "An experimental approach for the direct measurement of temperatures in the vicinity of the

keyhole front wall during deep-penetration laser welding," Appl. Sci. **10**, 3951.

Prashanth, K. G., S. Scudino, T. Maity, J. Das, and J. Eckert, 2017, "Is the energy density a reliable parameter for materials synthesis by selective laser melting?," Mater. Res. Lett. **5**, 386–390.

Qi, T., H. Zhu, H. Zhang, J. Yin, L. Ke, and X. Zeng, 2017, "Selective laser melting of Al7050 powder: Melting mode transition and comparison of the characteristics between the keyhole and conduction mode," Mater. Des. **135**, 257–266.

Rai, R., J. W. Elmer, T. A. Palmer, and T. DebRoy, 2007, "Heat transfer and fluid flow during keyhole mode laser welding of tantalum, Ti–6Al–4V, 304L stainless steel and vanadium," J. Phys. D **40**, 5753.

Ramirez-San-Juan, J. C., E. Rodriguez-Aboytes, A. E. Martinez-Canton, O. Baldovino-Pantaleon, A. Robledo-Martinez, N. Korneev, and R. Ramos-Garcia, 2010, "Time-resolved analysis of cavitation induced by CW lasers in absorbing liquids," Opt. Express **18**, 8735–8742.

Roehling, T. T., R. Shi, S. A. Khairallah, J. D. Roehling, G. M. Guss, J. T. McKeown, and M. J. Matthews, 2020, "Controlling grain nucleation and morphology by laser beam shaping in metal additive manufacturing," Mater. Des. **195**, 109071.

Rubenchik, A. M., S. S. Wu, V. K. Kanz, M. M. LeBlanc, W. H. Lowdermilk, M. D. Rotter, and J. R. Stanley, 2014, "Temperature-dependent 780-nm laser absorption by engineering grade aluminum, titanium, and steel alloy surfaces," Opt. Eng. **53**, 122506.

Sames, W. J., F. A. List, S. Pannala, R. R. Dehoff, and S. S. Babu, 2016, "The metallurgy and processing science of metal additive manufacturing," Int. Mater. Rev. **61**, 315–360.

Sanaei, N., and A. Fatemi, 2021, "Defects in additive manufactured metals and their effect on fatigue performance: A state-of-the-art review," Prog. Mater. Sci. **117**, 100724.

Schmerr, Jr., L. W., 2016, *Fundamentals of Ultrasonic Nondestructive Evaluation: A Modeling Approach*, Springer Series in Measurement Science and Technology (Springer, New York), https://link.springer.com/book/10.1007/978-3-319-30463-2.

Scime, L., and J. Beuth, 2019a, "Melt pool geometry and morphology variability for the Inconel 718 alloy in a laser powder bed fusion additive manufacturing process," Addit. Manuf. **29**, 100830.

Scime, L., and J. Beuth, 2019b, "Using machine learning to identify *in-situ* melt pool signatures indicative of flaw formation in a laser powder bed fusion additive manufacturing process," Addit. Manuf. **25**, 151–165.

Scipioni Bertoli, U., G. Guss, S. Wu, M. J. Matthews, and J. M. Schoenung, 2017, "*In-situ* characterization of laser-powder interaction and cooling rates through high-speed imaging of powder bed fusion additive manufacturing," Mater. Des. **135**, 385–396.

Scipioni Bertoli, U., A. J. Wolfer, M. J. Matthews, J.-P. R. Delplanque, and J. M. Schoenung, 2017, "On the limitations of volumetric energy density as a design parameter for selective laser melting," Mater. Des. **113**, 331–340.

Seltzman, A. H., and S. J. Wukitch, 2021, "Resolution and geometric limitations in laser powder bed fusion additively manufactured GRCop-84 structures for a lower hybrid current drive launcher," Fusion Eng. Des. **173**, 112847.

Selva, B., V. Miralles, I. Cantat, and M.-C. Jullien, 2010, "Thermocapillary actuation by optimized resistor pattern: Bubbles and droplets displacing, switching and trapping," Lab Chip **10**, 1835–1840.

Semak, V., and A. Matsunawa, 1997, "The role of recoil pressure in energy balance during laser materials processing," J. Phys. D **30**, 2541–2552.

Shevchik, S. A., C. Kenel, C. Leinenbach, and K. Wasmer, 2018, "Acoustic emission for *in situ* quality monitoring in additive manufacturing using spectral convolutional neural networks," Addit. Manuf. **21**, 598–604.

Shevchik, S. A., G. Masinelli, C. Kenel, C. Leinenbach, and K. Wasmer, 2019, "Deep learning for *in situ* and real-time quality monitoring in additive manufacturing using acoustic emission," IEEE Trans. Industr. Inform. **15**, 5194–5203.

Shu, Y., D. Galles, O. A. Tertuliano, B. A. McWilliams, N. Yang, W. Cai, and A. J. Lew, 2021, "A critical look at the prediction of the temperature field around a laser-induced melt pool on metallic substrates," Sci. Rep. **11**, 12224.

Simonds, B. J., J. Sowards, J. Hadler, E. Pfeif, B. Wilthan, J. Tanner, C. Harris, P. Williams, and J. Lehman, 2018, "Time-Resolved Absorptance and Melt Pool Dynamics during Intense Laser Irradiation of a Metal," Phys. Rev. Applied **10**, 044061.

Simonds, B. J., J. Tanner, A. Artusio-Glimpse, P. A. Williams, N. Parab, C. Zhao, and T. Sun, 2020, "Simultaneous high-speed x-ray transmission imaging and absolute dynamic absorptance measurements during high-power laser-metal processing," Procedia CIRP **94**, 775–779.

Simonds, B. J., J. Tanner, A. Artusio-Glimpse, P. A. Williams, N. Parab, C. Zhao, and T. Sun, 2021, "The causal relationship between melt pool geometry and energy absorption measured in real time during laser-based manufacturing," Appl. Mater. Today **23**, 101049.

Sing, S. L., J. An, W. Y. Yeong, and F. E. Wiria, 2016, "Laser and electron-beam powder-bed additive manufacturing of metallic implants: A review on processes, materials and designs," J. Orthop. Res. **34**, 369–385.

Sing, S. L., S. Huang, G. D. Goh, G. L. Goh, C. F. Tey, J. H. K. Tan, and W. Y. Yeong, 2021, "Emerging metallic systems for additive manufacturing: *In-situ* alloying and multi-metal processing in laser powder bed fusion," Prog. Mater. Sci. **119**, 100795.

Slotwinski, J. A., and E. J. Garboczi, 2015, "Metrology needs for metal additive manufacturing powders" JOM **67**, 538–543.

Snow, Z., A. R. Nassar, and E. W. Reutzel, 2020, "Invited review article: Review of the formation and impact of flaws in powder bed fusion additive manufacturing," Addit. Manuf. **36**, 101457.

Sofinowski, K. A., S. Raman, X. Wang, B. Gaskey, and M. Seita, 2021, "Layer-wise engineering of grain orientation (LEGO) in laser powder bed fusion of stainless steel 316L," Addit. Manuf. **38**, 101809.

Sun, S.-H., T. Ishimoto, K. Hagihara, Y. Tsutsumi, T. Hanawa, and T. Nakano, 2019, "Excellent mechanical and corrosion properties of austenitic stainless steel with a unique crystallographic lamellar microstructure via selective laser melting," Scr. Mater. **159**, 89–93.

Tan, W., N. S. Bailey, and Y. C. Shin, 2013, "Investigation of keyhole plume and molten pool based on a three-dimensional dynamic model with sharp interface formulation," J. Phys. D **46**, 055501.

Tang, M., P. C. Pistorius, and J. L. Beuth, 2017, "Prediction of lack-of-fusion porosity for powder bed fusion," Addit. Manuf. **14**, 39–48.

Tenbrock, C., F. G. Fischer, K. Wissenbach, J. H. Schleifenbaum, P. Wagenblast, W. Meiners, and J. Wagner, 2020, "Influence of keyhole and conduction mode melting for top-hat shaped beam profiles in laser powder bed fusion," J. Mater. Process. Technol. **278**, 116514.

Thampy, V., *et al.*, 2020, "Subsurface cooling rates and microstructural response during laser based metal additive manufacturing," Sci. Rep. **10**, 1981.

Thijs, L., K. Kempen, J.-P. Kruth, and J. Van Humbeeck, 2013, "Fine-structured aluminium products with controllable texture by selective laser melting of pre-alloyed AlSi10Mg powder," Acta Mater. **61**, 1809–1819.

Thijs, L., F. Verhaeghe, T. Craeghs, J. Van Humbeeck, and J. P. Kruth, 2010, "A study of the microstructural evolution during selective laser melting of Ti–6Al–4V," Acta Mater. **58**, 3303–3312.

Thomas, D., 2016, "Costs, benefits, and adoption of additive manufacturing: A supply chain perspective," Int. J. Adv. Manuf. Technol. **85**, 1857–1876.

Todaro, C. J., M. A. Easton, D. Qiu, D. Zhang, M. J. Bermingham, E. W. Lui, M. Brandt, D. H. StJohn, and M. Qian, 2020, "Grain structure control during metal 3D printing by high-intensity ultrasound," Nat. Commun. **11**, 142.

Tolochko, N. K., S. E. Mozzharov, I. A. Yadroitsev, T. Laoui, L. Froyen, V. I. Titov, and M. B. Ignatiev, 2004, "Balling processes during selective laser treatment of powders," Rapid Prototyp. J. **10**, 78–87.

Trapp, J., A. M. Rubenchik, G. Guss, and M. J. Matthews, 2017, "*In situ* absorptivity measurements of metallic powders during laser powder-bed fusion additive manufacturing," Appl. Mater. Today **9**, 341–349.

Verhaeghe, F., T. Craeghs, J. Heulens, and L. Pandelaers, 2009, "A pragmatic model for selective laser melting with evaporation," Acta Mater. **57**, 6006–6012.

Voisin, T., J. B. Forien, A. Perron, S. Aubry, N. Bertin, A. Samanta, A. Baker, and Y. M. Wang, 2021, "New insights on cellular structures strengthening mechanisms and thermal stability of an austenitic stainless steel fabricated by laser powder-bed-fusion," Acta Mater. **203**, 116476.

Wang, L., Y. Zhang, and W. Yan, 2020, "Evaporation Model for Keyhole Dynamics during Additive Manufacturing of Metal," Phys. Rev. Applied **14**, 064039.

Wang, X., L. N. Carter, B. Pang, M. M. Attallah, and M. H. Loretto, 2017, "Microstructure and yield strength of SLM-fabricated CM247LC Ni-superalloy," Acta Mater. **128**, 87–95.

Wang, X., S. Xu, S. Zhou, W. Xu, M. Leary, P. Choong, M. Qian, M. Brandt, and Y. M. Xie, 2016, "Topological design and additive manufacturing of porous metals for bone scaffolds and orthopaedic implants: A review," Biomaterials **83**, 127–141.

Wang, Y., X. Liu, K. S. Im, W.-K. Lee, J. Wang, K. Fezzaa, D. L. S. Hung, and J. R. Winkelman, 2008, "Ultrafast x-ray study of dense-liquid-jet flow dynamics using structure-tracking velocimetry," Nat. Phys. **4**, 305–309.

Wang, Y. M., *et al.*, 2018, "Additively manufactured hierarchical stainless steels with high strength and ductility," Nat. Mater. **17**, 63–71.

Wei, H. L., J. W. Elmer, and T. DebRoy, 2017, "Crystal growth during keyhole mode laser welding," Acta Mater. **133**, 10–20.

Wei, M., W. J. Ding, G. Vastola, and Y.-W. Zhang, 2022, "Quantitative study on the dynamics of melt pool and keyhole and their controlling factors in metal laser melting," Addit. Manuf. **54**, 102779.

Weingarten, C., D. Buchbinder, N. Pirch, W. Meiners, K. Wissenbach, and R. Poprawe, 2015, "Formation and reduction of hydrogen porosity during selective laser melting of AlSi10Mg," J. Mater. Process. Technol. **221**, 112–120.

Wellershoff, S. S., J. Hohlfeld, J. Güdde, and E. Matthias, 1999, "The role of electron-phonon coupling in femtosecond laser damage of metals," Appl. Phys. A **69**, S99–S107.

Wilkins, S. W., T. E. Gureyev, D. Gao, A. Pogany, and A. W. Stevenson, 1996, "Phase-contrast imaging using polychromatic hard x-rays," Nature (London) **384**, 335–338.

Williams, P., J. Hadler, F. Maring, R. Lee, K. Rogers, B. Simonds, M. Spidell, M. Stephens, A. Feldman, and J. Lehman, 2017, "Portable, high-accuracy, non-absorbing laser power measurement at kilowatt levels by means of radiation pressure," Opt. Express **25**, 4382–4392.

Williams, P. A., K. A. Rogers, J. A. Hadler, A. B. Artusio-Glimpse, and J. H. Lehman, 2021, "Axial force radiometer for primary standard laser power measurements using photon momentum," Metrologia **58**, 015010.

Wolff, S. J., H. Wu, N. Parab, C. Zhao, K. F. Ehmann, T. Sun, and J. Cao, 2019, "*In-situ* high-speed x-ray imaging of piezo-driven directed energy deposition additive manufacturing," Sci. Rep. **9**, 962.

Wu, A. S., D. W. Brown, M. Kumar, G. F. Gallegos, and W. E. King, 2014, "An experimental investigation into additive manufacturing-induced residual stresses in 316L stainless steel," Metall. Mater. Trans. A **45**, 6260–6270.

Wu, Z., S. P. Narra, and A. Rollett, 2020, "Exploring the fabrication limits of thin-wall structures in a laser powder bed fusion process," Int. J. Adv. Manuf. Technol. **110**, 191–207.

Yadroitsev, I., P. Krakhmalev, and I. Yadroitsava, 2014, "Selective laser melting of Ti6Al4V alloy for biomedical applications: Temperature monitoring and microstructural evolution," J. Alloys Compd. **583**, 404–409.

Yan, W., Y. Lu, K. Jones, Z. Yang, J. Fox, P. Witherell, G. Wagner, and W. K. Liu, 2020, "Data-driven characterization of thermal models for powder-bed-fusion additive manufacturing," Addit. Manuf. **36**, 101503.

Yang, J., H. Yu, J. Yin, M. Gao, Z. Wang, and X. Zeng, 2016, "Formation and control of martensite in Ti-6Al-4V alloy produced by selective laser melting," Mater. Des. **108**, 308–318.

Yang, K. V., P. Rometsch, T. Jarvis, J. Rao, S. Cao, C. Davies, and X. Wu, 2018, "Porosity formation mechanisms and fatigue response in Al-Si-Mg alloys made by selective laser melting," Mater. Sci. Eng. A **712**, 166–174.

Ye, J., S. A. Khairallah, A. M. Rubenchik, M. F. Crumb, G. Guss, J. Belak, and M. J. Matthews, 2019, "Energy coupling mechanisms and scaling behavior associated with laser powder bed fusion additive manufacturing," Adv. Eng. Mater. **21**, 1900185.

Zhang, B., S. Liu, and Y. C. Shin, 2019, "In-process monitoring of porosity during laser additive manufacturing process," Addit. Manuf. **28**, 497–505.

Zhang, H., H. Zhu, X. Nie, J. Yin, Z. Hu, and X. Zeng, 2017, "Effect of zirconium addition on crack, microstructure and mechanical behavior of selective laser melted Al-Cu-Mg alloy," Scr. Mater. **134**, 6–10.

Zhao, C., K. Fezzaa, R. W. Cunningham, H. Wen, F. De Carlo, L. Chen, A. D. Rollett, and T. Sun, 2017, "Real-time monitoring of laser powder bed fusion process using high-speed x-ray imaging and diffraction," Sci. Rep. **7**, 3602.

Zhao, C., Q. Guo, X. Li, N. Parab, K. Fezzaa, W. Tan, L. Chen, and T. Sun, 2019, "Bulk-Explosion-Induced Metal Spattering during Laser Processing," Phys. Rev. X **9**, 021052.

Zhao, C., N. D. Parab, X. Li, K. Fezzaa, W. Tan, A. D. Rollett, and T. Sun, 2020, "Critical instability at moving keyhole tip generates porosity in laser melting," Science **370**, 1080–1086.

Zhao, C., Y. Yang, B. Shi, W. Shao, and S. Chen, 2022, "*Operando* monitoring microstructures and defects in laser fusion additive manufacturing of metals," Chin. Sci. Bull. **67**, 3036–3053.

Zhao, H., and T. DebRoy, 2003, "Macroporosity free aluminum alloy weldments through numerical simulation of keyhole mode laser welding," J. Appl. Phys. **93**, 10089–10096.

Zhu, J. N., E. Borisov, X. Liang, E. Farber, M. J. M. Hermans, and V. A. Popovich, 2021, "Predictive analytical modelling and experimental validation of processing maps in additive manufacturing of nitinol alloys," Addit. Manuf. **38**, 101802.

Zhu, Q., Z. Liu, and J. Yan, 2021, "Machine learning for metal additive manufacturing: Predicting temperature and melt pool fluid dynamics using physics-informed neural networks," Comput. Mech. **67**, 619–635.